Published in final edited form as:

Cell Rep. 2019 October 08; 29(2): 301–316.e10. doi:10.1016/j.celrep.2019.08.104.

Tau-Mediated Disruption of the Spliceosome Triggers Cryptic RNA Splicing and Neurodegeneration in Alzheimer's Disease

Yi-Chen Hsieh[1,11], **Caiwei Guo**[2,11], **Hari K. Yalamanchili**[3,11], **Measho Abreha**[4], **Rami Al-Ouran**[3], **Yarong Li**[5], **Eric B. Dammer**[4], **James J. Lah**[6], **Allan I. Levey**[6], **David A. Bennett**[7], **Philip L. De Jager**[8,9], **Nicholas T. Seyfried**[4,6], **Zhandong Liu**[3,10], **Joshua M. Shulman**[1,2,5,10,12,*]

[1]Department of Molecular and Human Genetics, Baylor College of Medicine, Houston, TX 77030, USA

[2]Department of Neuroscience, Baylor College of Medicine, Houston, TX 77030, USA

[3]Department of Pediatrics, Baylor College of Medicine, Houston, TX 77030, USA

[4]Department of Biochemistry, Emory University School of Medicine, Atlanta, GA 30322, USA

[5]Department of Neurology, Baylor College of Medicine, Houston, TX 77030, USA

[6]Department of Neurology, Emory University School of Medicine, Atlanta, GA 30322, USA

[7]Rush Alzheimer's Disease Center, Rush University Medical Center, Chicago, IL 60612, USA

[8]Center for Translational and Computational Neuroimmunology, Department of Neurology, Columbia University Medical Center, New York, NY 10032, USA

[9]Cell Circuits Program, Broad Institute, Cambridge, MA 02142, USA

[10]Jan and Dan Duncan Neurological Research Institute, Texas Children's Hospital, Houston, TX 77030, USA

[11]These authors contributed equally

[12]Lead Contact

SUMMARY

In Alzheimer's disease (AD), spliceosomal proteins with critical roles in RNA processing aberrantly aggregate and mislocalize to Tau neurofibrillary tangles. We test the hypothesis that

*Correspondence: joshua.shulman@bcm.edu.

AUTHOR CONTRIBUTIONS

Conceptualization, Y.-C.H., C.G., H.K.Y., M.A., N.T.S., Z.L., and J.M.S.; Investigation, Y.-C.H., C.G., M.A., and Y.L.; Methodology, H.K.Y. and Z.L.; Formal Analysis, Y.-C.H., C.G., H.K.Y., R.A.-L., and E.B.D.; Data Curation, H.K.Y. and R.A.-L.; Writing - Original Draft, Y.-C.H., C.G., and J.M.S.; Writing - Review and Editing, Y.-C.H., C.G., H.K.Y., M.A, R.A.-L., E.B.D, Y.L., J.J.L., A.I.L., D.A.B., P.L.D.J., N.T.S., J.M.S., and Z.L.; Funding Acquisition, J.J.L., A.I.L., D.A.B., P.L.D.J., N.T.S., J.M.S., and Z.L.; Resources, D.A.B. and P.L.D.J.; Supervision, N.T.S, J.M.S., and Z.L.

DECLARATION OF INTERESTS

The authors declare no competing interests.

SUPPLEMENTAL INFORMATION

Supplemental Information can be found online at https://doi.org/10.1016/j.celrep.2019.08.104.

Tau-spliceosome interactions disrupt pre-mRNA splicing in AD. In human postmortem brain with AD pathology, Tau coimmunoprecipitates with spliceosomal components. In *Drosophila*, pan-neuronal Tau expression triggers reductions in multiple core and U1-specific spliceosomal proteins, and genetic disruption of these factors, including SmB, U1–70K, and U1A, enhances Tau-mediated neurodegeneration. We further show that loss of function in *SmB*, encoding a core spliceosomal protein, causes decreased survival, progressive locomotor impairment, and neuronal loss, independent of Tau toxicity. Lastly, RNA sequencing reveals a similar profile of mRNA splicing errors in *SmB* mutant and Tau transgenic flies, including intron retention and non-annotated cryptic splice junctions. In human brains, we confirm cryptic splicing errors in association with neurofibrillary tangle burden. Our results implicate spliceosome disruption and the resulting transcriptome perturbation in Tau-mediated neurodegeneration in AD.

In Brief

Integrating studies of human postmortem brain tissue and *Drosophila melanogaster* models, Hsieh et al. show that Alzheimer's disease Tau neurofibrillary tangle pathology disrupts spliceosome activity. RNA-splicing errors, including intron retention and non-annotated cryptic junctions, and resulting transcriptome perturbation are implicated in Tau-mediated neurodegenerative mechanisms.

Graphical Abstract

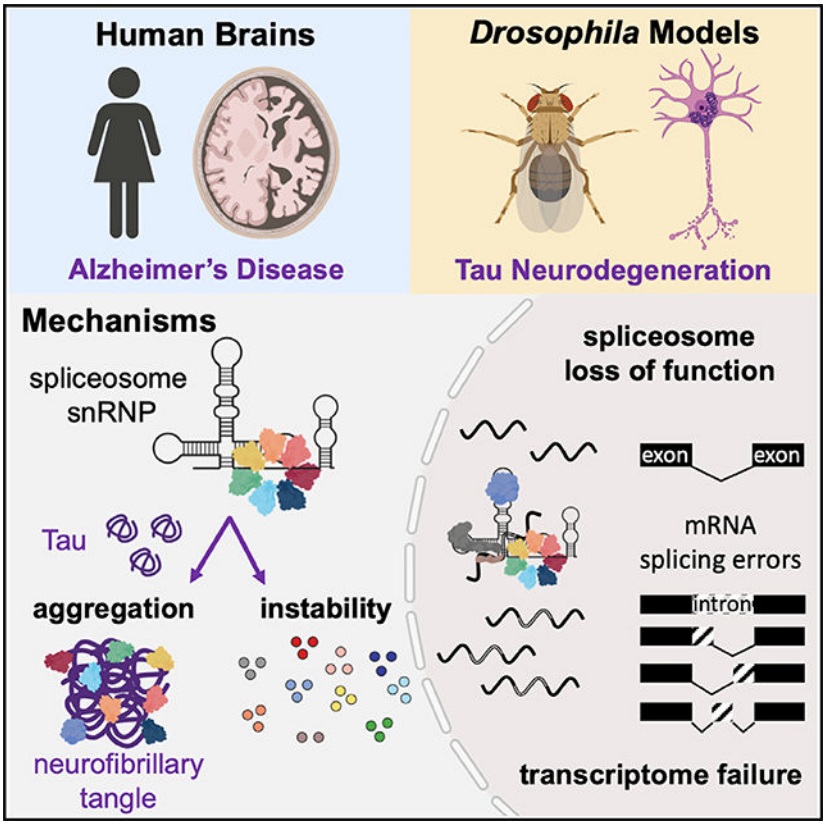

INTRODUCTION

In eukaryotes, precursor mRNA (pre-mRNA) splicing removes introns and generates mature mRNA transcripts, subserving a critical role in the regulation of gene expression. Splicing contributes to neuronal transcriptional diversity and function, and disruption of splicing mechanisms causes neurologic disease (Cooper et al., 2009; Tollervey et al., 2011). For example, spinal muscular atrophy is caused by mutations in the *survival motor neuron (SMN)* gene, which initiates assembly of the spliceosome, the molecular machine responsible for pre-mRNA splicing (Lefebvre et al., 1995; Lorson et al., 1999). Mutation of other RNA-binding proteins implicated in splicing, including the TAR DNA-binding protein 43 (TDP-43) and fused in sarcoma (FUS), are associated with frontotemporal dementia and amyotrophic lateral sclerosis (FTD-ALS) (Neumann et al., 2006; Sreedharan et al., 2008; Vance et al., 2009). In experimental mouse models, loss of function in spliceosomal components is also associated with neurodegenerative phenotypes (Jia et al., 2012; Ling et al., 2015; Polymenidou et al., 2011; Tan et al., 2016; Zhang et al., 2008).

The major spliceosome is composed of five small nuclear ribonucleoprotein particle (snRNP) complexes (U1, U2, U4, U5, and U6), each including a small nuclear RNA (snRNA), seven Sm proteins (or Lsm proteins in U6), and specific factors, such as U1–70K, U1A, and U1C for the U1 snRNP (Will and Lührmann, 2011). Assembly begins with the formation of the core snRNA-Sm protein complex in the cytoplasm, followed by nuclear import and subsequent incorporation of specific proteins to generate the mature snRNP. Pre-mRNA splicing is initiated by recognition of 5′ splice sites by the U1 snRNP, followed by dynamic interactions with other snRNP complexes. Disruption of spliceosomal factors, either in cell culture or mouse genetic models, induces widespread mRNA splicing errors, including intron retention and cryptic junctions—consisting of non-conserved, non-annotated splice junctions (Humphrey et al., 2017; Jia et al., 2012; Kaida et al., 2010; Ling et al., 2015; Polymenidou et al., 2011; Tan et al., 2016; Zhang et al., 2008). Cryptic splicing has also been documented in human postmortem brain from individuals with TDP-43 mutations (Ling et al., 2015). Emerging evidence suggests that disrupted assembly of RNA-binding protein complexes, such as the spliceosome, may promote FTD-ALS pathogenesis (Ito et al., 2017; Lee et al., 2016a; Yin et al., 2017).

Tau protein, encoded by the *microtubule associated protein tau (MAPT)* gene, aggregates to form neurofibrillary tangles, characteristic of Alzheimer's disease (AD) and other tauopathies. Neurofibrillary tangle pathologic burden is strongly correlated with cognitive decline in AD (Arriagada et al., 1992; Braak and Braak, 1991; Gómez-Isla et al., 1997), and soluble, oligomeric forms of Tau are also implicated in synaptic dysfunction and neuronal death (Cowan and Mudher, 2013; Spires-Jones and Hyman, 2014). In human AD postmortem brain tissue, multiple core and specific components of the U1 snRNP co-aggregate with Tau in neurofibrillary tangles (Bai et al., 2013; Hales et al., 2014), and similar findings have been reported in *MAPT* transgenic mice (Maziuk et al., 2018; Vanderweyde et al., 2016) and *in vitro* (Bishof et al., 2018). Consistent with these observations, evidence of altered splicing in AD has also recently emerged (Bai et al., 2013; Raj et al., 2018). Independently, in a screen of candidate genes from AD-associated human genomic loci, we discovered that *SmB*, the fly ortholog of human *SNRPN* (encoding SmN),

modulates Tau-mediated neurotoxicity (Shulman et al., 2014). Here, we couple studies in human autopsy cohorts and *Drosophila* models to further investigate the hypothesis that Tau-spliceosome interactions lead to splicing errors and, ultimately, neurodegeneration in AD.

RESULTS

Tau Associates with Numerous snRNP Core Components in Human Brains with AD Pathology

We previously showed that multiple core and U1-specific components of the spliceosome are enriched in insoluble protein fractions and closely associate with neurofibrillary tangles in AD postmortem brain tissue (Bai et al., 2013; Bishof et al., 2018; Hales et al., 2014). To further explore the potential for interactions with soluble, oligomeric forms of Tau that most likely mediate toxicity, we performed immunoaffinity-purification coupled to mass spectrometry. A Tau monoclonal antibody (Tau5) was used for immunoprecipitation from human brain lysate soluble fractions, prepared from either AD or non-demented control autopsy cases (n = 4 each; Table S1), and normalized for total protein levels. As a negative control, we performed immunoprecipitation with a non-specific immunoglobulin G (IgG) from pooled control and AD inputs. Tau immunoprecipitation was confirmed by western blot analysis (Figure S1A). Next, samples were on-bead digested and peptides analyzed by liquid chromatography-tandem mass spectrometry using label-free quantitation. Our analysis identified 1,065 proteins across all samples. Differential enrichment analysis of Tau-interacting partners identified 513 proteins enriched in AD versus control brains ($p < 0.05$, fold-change > 1.5; Data S1, tab i), highlighting proteins with significantly altered interactions in the context of AD pathology (Figure 1A). Among those proteins characterized by increased affinity for Tau in AD are numerous ribonucleoproteins ($p = 7.7 \times 10^{-5}$) based on Gene Ontology (GO) enrichment analysis, with roles in mRNA processing, including splicing and/or translation (Figures 1A and S1C; Data S1, tabs i and ii). Among these, nine spliceosome proteins, including SNRNP70 (U1–70K), SNRPD2 (SmD2), SNRPD3 (SmD3), SNRPN (SmN), and SNRPA (U1A), each exhibited more than 6-fold increased affinity to Tau in AD brains versus control (Figure S1B). These data suggest that, in AD, soluble forms of Tau may associate with spliceosome components, possibly preceding the formation of neurofibrillary tangles.

Tau Genetically Interacts with Multiple Core Spliceosome Components in *Drosophila*

Expression of human *MAPT* in *Drosophila* is neurotoxic, including either wild-type *Tau* (Tau^{WT}) or mutant forms associated with familial frontotemporal dementia. We initially selected a mutant Tau^{V337M} transgenic fly strain, which is amenable to sensitive and robust detection of genetic modifiers (Shulman and Feany, 2003; Shulman et al., 2011, 2014). Using the *GMR-GAL4* driver, we directed expression of Tau to the *Drosophila* retina, along with RNAi transgenes targeting 10 distinct U1 snRNP components, including the Sm core (SmB, SmD1, SmD2, SmD3, SmE, SmF, and SmG) and U1-specific factors (U1–70K, U1C, and U1A). We required consistent interactions with at least two independent lines to minimize off-target effects and excluded RNAi strains with evidence of significant retinal toxicity in the absence of Tau (Data S1, tab iii). These experiments confirmed our prior results with *SmB* (Shulman et al., 2014) and additionally revealed that knockdown of fly

homologs of *SmD2, U1–70K, U1C*, and *SmE* similarly enhance Tau-induced retinal degeneration, causing reduced eye size and increased, roughened appearance (all $p < 0.0001$; Figure 1B). We next employed a complementary assay in which *Tau* expression is restricted to adult photoreceptors, using the *Rhodopsin 1 (Rh1)-GAL4* driver, causing an age-dependent, progressive loss of the light-induced depolarization response, but preserved retinal morphology (Chouhan et al., 2016). Based on the electroretinogram (ERG), we confirmed that RNAi knockdown of U1 snRNP components showed consistent enhancement of the *Rh1 > Tau^{WT}* functional degenerative phenotype (Figure S2A). To further examine for dose-sensitive genetic interactions, we also tested available mutant alleles, including null alleles for fly *snRNP-U1–70K* and *sans-fille (snf*, an ortholog of U1A) (Flickinger and Salz, 1994; Salz et al., 2004) or a newly generated *SmB* hypomorphic allele (*SmB^{MG}*; see below). The Tau ERG phenotype was dominantly enhanced in either an *SmB$^{MG/+}$* (Figure 1C) or *snf$^{+/-}$* heterozygous genetic background (Figure S2B) but not in *snRNP-U1–70K$^{+/-}$* (Figure S2C), whereas control heterozygous animals had normal ERGs in the absence of Tau.

Next, we expressed Tau pan-neuronally using the *elav-GAL4* driver line, which causes age-dependent neuronal loss and histologic changes in the adult brain (Wittmann et al., 2001). RNAi knockdown of U1 snRNP genes using *elav-GAL4* resulted in embryonic lethality, so we again took advantage of the available mutant alleles to examine for dominant genetic interactions. In 10-day-old animals, *elav > Tau^{R406W}* causes a mild degree of neurodegenerative changes, based on the accumulation of vacuoles on hematoxylin and eosin-stained, paraffin brain sections (Figure 1D). By contrast, Tau-induced neurodegeneration was dominantly enhanced in either an *SmB$^{MG/+}$* (Figure 1D) or *snRNP-U1–70K$^{+/-}$* (Figures S2D and S2E) heterozygous genetic background, but not in *snf$^{+/-}$*. We did not detect evidence of neurodegeneration in heterozygous *SmB* or *snRNP-U1–70K* control flies independent of Tau (Figures 1D and S2E). In sum, based on multiple independent assays, our data suggest that genetic manipulation of U1 snRNP components can enhance Tau-induced neurodegenerative phenotypes in *Drosophila.* We previously reported that overexpression of *SmB* suppresses the Tau rough eye phenotype (Shulman et al., 2014). However, we were unable to confirm consistent suppression of Tau-induced vacuolar degeneration in the adult brain (Figure S2F). If Tau disrupts the function of multiple spliceosome proteins, it is possible that overexpression of one factor in isolation (e.g., SmB) is not sufficient to rescue Tau toxicity in all contexts (discussed further below).

Tau-Induced Spliceosome Disruption in *Drosophila*

We next examined the expression of core and U1-specific spliceosomal proteins in the brains of Tau transgenic flies (*elav > Tau^{R406W}*). We focused on 1-day-old adults preceding the onset of significant neuronal loss (Wittmann et al., 2001). Based on western blots prepared from adult head total protein homogenates, *elav > Tau^{R406W}* flies demonstrate an approximately 30%−50% reduction in the levels of multiple core (SmB, SmD3) and U1-specific (U1A/SNF and U1–70K) spliceosomal components when compared to *elav-GAL4/+* controls, whereas SmD2 was increased (Figures 2A and 2B). Based on quantitative real-time PCR, mRNA levels were not significantly altered for three out of five spliceosomal factors (*SmB, SmD3*, and *snf)*, consistent with a post-transcriptional mechanism for the observed protein reductions (Figure 2C). In addition, immunofluorescence staining of adult

brains using the anti-Sm antibody (Y12), which recognizes both SmB and SmD3 in *Drosophila* (Brahms et al., 2000; Gonsalvez et al., 2006), or an anti-U1A antibody confirmed significantly reduced U1 snRNP levels and depletion from neuronal nuclei (Figures 2D and 2E).

In human AD postmortem brain tissue, multiple spliceosomal proteins can be found mislocalized to the cytoplasm, co-aggregating with Tau in neurofibrillary tangles (Bai et al., 2013; Hales et al., 2014). In *Drosophila* neurons, although Tau is misfolded and hyperphosphorylated as in human AD, it remains predominantly soluble and oligomeric (Ali et al., 2012; Cowan et al., 2010; Mudher et al., 2004; Wittmann et al., 2001). In other human tauopathies, such as corticobasal degeneration, fibrillar Tau inclusions are observed in both neurons and glia, and prior work has established that Tau aggregates more readily when expressed in *Drosophila* glia, forming insoluble, tangle-like, cytoplasmic inclusions (Colodner and Feany, 2010). As a complementary approach, we therefore stained for Sm proteins in a *Drosophila* glial tauopathy model, which relies on the *repo-GAL4* glial driver. Indeed, aged *repo > Tau^{WT}* flies manifest numerous cytoplasmic aggregates costaining for both phospho-Tau (anti-pSer214) and SmB/SmD3 (Y12) (Figure 2F). Consistent with this, on western blots, we can detect both Tau and increased SmB protein in insoluble fractions prepared from *repo > Tau^{WT}* heads (Figure S3B). Together, our results suggest that soluble Tau species lead to a loss of snRNP protein levels, whereas insoluble forms of Tau coaggregate with spliceosomal proteins, leading to cytoplasmic sequestration.

Spliceosome Loss of Function Causes Neurodegeneration

Our data suggest that pathological forms of Tau can trigger a reduction in core and U1-specific spliceosomal components in *Drosophila* neurons, and that further experimental reduction of these proteins enhances Tau-induced neurodegeneration. We next examined whether disruption of the U1 snRNP is sufficient to cause neurodegeneration, independent of transgenic Tau. The spliceosome is essential for organismal development and maintenance of cellular functions. Available null or strong hypomorphic alleles for U1 snRNP components including *snf/U1A, snRNP-U1–70K*, and *SmB* are embryonic lethal (Anne, 2010; Flickinger and Salz, 1994; Salz et al., 2004), hindering studies in the adult nervous system. *Drosophila SmB* is the single fly ortholog for both human *SNRPB* and *SNRPN*, which substitutes for SmB in neurons (McAllister et al., 1988; Saltzman et al., 2011). While attempting to generate a GFP-tagged allele of fly *SmB*, we serendipitously created a viable, hypomorphic allele. *SmB^{MI07584}* contains a Minos-mediated integration cassette (MiMIC) transposable element insertion within the first intron of *SmB* (Venken et al., 2011) (Figure 3A). Using recombinase-mediated cassette exchange, the MiMIC element was replaced with a GFP coding exon flanked by splice acceptor and donor sequences (Nagarkar-Jaiswal et al., 2015a, 2015b). Hereafter, we refer to this allele as *SmB^{MG}* for MiMIC-GFP. The *SmB^{MG}* allele, encoding a full-length, N-terminal GFP-tagged SmB protein, is homozygous viable. In adult brains, the SmB^{MG} fusion protein is expressed at comparable levels to SmB in wild-type controls (Figure 3B) and is localized to the nucleus, as expected (Figure 3C). Surprisingly however, *SmB^{MG}* fails to complement several available *SmB* loss-of-function alleles, including *SmB^{MI07584}*, *SmB^{BG02775}*, *SmB^{SH0509}*, or a deficiency strain covering the locus (*Df(2L)BSC453;* Figure 3A), causing embryonic lethality in compound heterozygotes

(Table S2). Viability is fully rescued by a 90-kb bacterial artificial chromosome (BAC) transgenic construct including the *SmB* genomic locus (*SmB*^{GR}; Figure 3A). These data suggest that *SmB*^{MG} is a viable, hypomorphic allele encoding an SmB protein with reduced function, yet is sufficient for embryonic development and adult viability.

We first examined survival and locomotor behavior in *SmB*$^{MG/MG}$ adults, since these phenotypes have previously been associated with neurodegeneration, including in Tau transgenic flies (Lessing and Bonini, 2009; Mudher et al., 2004; Wittmann et al., 2001). Indeed, *SmB* loss of function caused reduced survival (Figures 3D and S4A) and age-dependent, progressive locomotor impairment, based on the startle-induced, negative geotaxis assay (climbing) (Figures 3E and S4B). These *SmB*$^{MG/MG}$ phenotypes were rescued by the *SmB* genomic construct (*SmB*$^{MG/MG}$; *SmB*^{GR}*/+)*, establishing specificity. In addition, the *SmB*$^{MG/MG}$ survival and locomotor phenotypes were rescued by pan-neuronal expression of a wild-type *SmB* cDNA (*elav* > *SmB*), suggesting that these phenotypes arise from reduced *SmB* function in neurons (Figures 3F and 3G). In sum, our data indicate that SmB is required for maintenance of nervous system function and survival with aging.

Next, we investigated for more direct evidence of neurodegeneration in *SmB*$^{MG/MG}$ adult brains. Hematoxylin and eosin-stained paraffin sections revealed overall preserved adult brain morphology without overt evidence of neuropil vacuolar degenerative changes. We therefore examined specific, vulnerable cell populations previously reported in Tau transgenic and other *Drosophila* models of neurodegenerative disorders (Bardai et al., 2018; Ghosh and Feany, 2004; Khurana et al., 2010; Merlo et al., 2014). We first quantified cortical nuclei in the region of the mushroom body calyx, which is a hub for invertebrate learning and memory (Owald and Waddell, 2015). The cells in this region are predominantly neuronal, but also include sparse glia (Figure S4F). In *SmB*$^{MG/MG}$ flies, we discovered an age-dependent decline in cellular density (Figures 4A–4C). Cholinergic neurons are particularly susceptible to loss in both human AD and in *Drosophila* Tau transgenic models (Coyle et al., 1983; Wittmann et al., 2001). We found that *SmB*$^{MG/MG}$ similarly causes progressive cholinergic neuronal loss in the fly lamina, based on quantification using a choline-acetyl transferase (*ChAT*) > *Betagalactosidase* reporter (Figures 4D–4F). Finally, similar to Tau transgenic flies (Dias-Santagata et al., 2007), we documented cell death using the TUNEL assay in *SmB*$^{MG/MG}$ flies (Figures S4C–S4E). Importantly, introduction of the *SmB* genomic construct rescued all of the observed *SmB*$^{MG/MG}$ neurodegenerative phenotypes. We also confirmed that RNAi-mediated knockdown of *SmB* in neurons yields consistent results (Figure S5). Overall, our data suggest that loss of function of *SmB*, an essential, core spliceosome component, is sufficient to cause age-dependent neurodegeneration and progressive nervous system dysfunction.

Tau and Spliceosome Disruption Cause Similar Aberrant Splicing Signatures in *Drosophila* Brains

To determine if Tau is sufficient to cause splicing errors, possibly via interactions with the spliceosome, we performed RNA sequencing (RNA-seq) on heads from Tau transgenics (*elav* > *Tau*^{WT} and *elav* > *Tau*^{R406W}) or controls (*elav-GAL4/+).* Analyses were performed at 1, 10, or 20 days, to assess for potential changes relative to the onset and progression of

neurodegeneration. To examine the consequences of direct spliceosomal loss of function, RNA-seq was also performed on 10-day-old *SmB*$^{MG/MG}$ flies. We initially evaluated alternative splicing changes using the replicate Multivariate Analysis of Transcript Splicing (rMATS) tool (Shen et al., 2014). Indeed, we discovered up to 1,559 significant (false discovery rate [FDR] < 0.05), differential splicing events triggered by Tau expression in the adult fly brain (Figure S6A; Table S3; Data S2). Tau-associated splicing changes were present in 1-day-old animals, preceding the onset of neurodegenerative phenotypes, and were enhanced in flies expressing *Tau*^{R406W}, a mutant form causing familial frontotemporal dementia. Genetic disruption of the core spliceosomal factor, *SmB*, was associated with even stronger transcriptome perturbations, causing 16,424 differential splicing events in 10-day-old animals (Figure S6A; Table S3; Data S2).

These results are consistent with our hypothesis that Tau-spliceosome interactions may significantly alter the transcriptional landscape. However, in order to differentiate aberrant splicing errors from alternative splicing, we next applied two complementary analytic tools, including (1) a newly developed differential expression of intron (DEIn) algorithm and (2) the previously validated tool CrypSplice (Tan et al., 2016). DEIn uses a stringent definition of intron retention as transcribed sequences mapping to gene loci, but completely absent in the *Drosophila* transcriptome reference (Figure S6B), consistent with aberrant suppression of otherwise, constitutively spliced introns. By contrast, most intron retention events recognized by rMATS are documented alternative exons in annotated transcript isoforms. Similarly, CrypSplice facilitates sensitive detection of recurrent, cryptic splice junctions that are not present in annotated transcriptome references, causing shifts in either splice donor (5′) and/or acceptor (3′) positions, as well as new combinations of splice donors and acceptors (Figure 5A). For this work, the CrypSplice software was further enhanced to improve annotation of cryptic splicing errors to facilitate interpretation of both causal mechanisms and potential consequences (see below and the STAR Methods). Indeed, our analyses identify a substantial number of splicing errors in Tau transgenic flies, including up to 437 cryptic splice junctions and 1,138 intron retention events (Figure 5B; Tables S4 and S5; Data S1, tabs iv and v). As with the differential splicing analysis (above), splicing errors were detectable in 1-day-old animals before the manifestation of neurodegeneration and were more frequent in *Tau*^{R406W} than *Tau*^{WT} at all time points. Cryptic splicing errors also increased with aging at successive time points (Figure 5B). For each class of splicing error, we prioritized and successfully validated several DEIn and CrypSplice predictions by RT-PCR. In total, 7 out of 13 (54%) splicing errors were experimentally confirmed, including 3 of 7 cryptic splice junctions and 4 of 6 intron retention events. Schematic plots for three representative examples are highlighted in Figure 5C, and RT-PCR results are shown in Figure S6C.

To better understand the underlying mechanism(s), we next examined the profile of splicing errors detected in *Tau*^{R406W} transgenic flies, pooling results from all three time points and focusing on 592 genes harboring 985 cryptic splicing errors and 1,606 genes with 2,767 retained introns (Data S1, tabs vi and vii). Our analyses of *SmB* loss-of-function animals revealed comparable numbers of genes with recurrent splicing errors (608 or 2,446 genes affected by cryptic splicing or intron retention, respectively) (Figure 5B; Tables S4 and S5; Data S1, tabs iv and v). We found a 28% overlap in the specific genes affected by cryptic

splicing (39% overlap for intron retention), and these results were significantly greater than that expected due to chance ($p_{cryptic} = 7.7 \times 10^{-85}$ or $p_{intron} = 4.3 \times 10^{-89}$; Figure 5D). We obtained consistent results when analyzing overlap based on specific splice junctions or retained introns, rather than clustering by the affected gene ($p_{cryptic} = 0.001$ or $p_{intron} = 2.0 \times 10^{-24}$) (Figures S6D and S6F). Compared to all *Drosophila* genes, those vulnerable to splicing errors had significantly increased numbers of introns and more alternative splice forms ($p < 0.001$; Figure 5E), consistent with our hypothesis of disruption in the fundamental molecular machinery that mediates splicing of all introns, as expected due to a spliceosomal defect. Tau-induced cryptic splicing errors affected either the splice donor and/or acceptor sites (Figures 5A and 5B). Based on our experimental data suggesting that several spliceosomal proteins may be reduced and therefore dose limiting in Tau transgenic flies (Figure 2), we hypothesized that splicing errors might occur preferentially at annotated splice donor and/or acceptor sites that diverge from the U1 or U2 consensus binding sites, respectively. For this analysis, in order to avoid ambiguity and confidently infer the original annotated, apparently skipped, donor or acceptor sequences, it was only possible to consider cryptic splice errors causing either new splice donors or acceptors (Figure S7A and STAR Methods). Indeed, we found that the average estimated binding strength for these "error prone" splice donor and acceptor sites was significantly lower ($p < 0.001$) than for all annotated sites in the *Drosophila* genome; representative examples are highlighted in Figure 5F, and results of the transcriptome-wide analysis are presented in Figure S7B. Consistent results were also obtained for splice junctions flanking Tau-triggered intron retention events. Overall, our data suggest that Tau-induced splicing errors have a similar profile to *SmB* loss of function, consistent with a shared mechanism due to spliceosomal disruption.

Lastly, to understand the potential functional consequences, we further classified splicing errors based on their potential to disrupt protein expression. Indeed, 49% of cryptic splicing errors and 81% of intron retention events detected in Tau transgenic flies involve coding exons, potentially disrupting open reading frames (Figure 5G). Most of the remaining splicing errors are predicted to affect 5′-UTR sequences and may therefore impact mRNA stability and/or translation. Based on enrichment analysis for GO terms, Tau-induced cryptic splicing errors affected genes with predominant roles in protein phosphorylation ($p = 4.8 \times 10^{-6}$), synaptic vesicle exocytosis ($p = 3.4 \times 10^{-4}$), and neurotransmitter transport ($p = 3.4 \times 10^{-4}$), whereas Tau-induced intron retention affected genes implicated in the innate immune response ($p = 1.0 \times 10^{-10}$) and oxidation reduction ($p = 1.8 \times 10^{-5}$) (Data S1, tab viii). Overall, our data suggest that Tau-induced splicing errors likely have a broad impact on the *Drosophila* brain transcriptome—with potential consequences for CNS function and maintenance—and cause a profile similar to genetic disruption of *SmB*, encoding a core spliceosomal factor.

Tau Pathology Is Associated with Cryptic Splicing Errors in Human Brains

Recent studies of human postmortem brain have identified mRNA splicing changes, including intron retention, in the setting of AD pathology (Bai et al., 2013; Raj et al., 2018). To determine if Tau neuropathology in AD is additionally associated with cryptic splicing errors, we leveraged data from the Religious Orders Study and Rush Memory and Aging Project (ROSMAP) (Bennett et al., 2018; Mostafavi et al., 2018). Our analyses included 620

deceased subjects with comprehensive clinical and pathologic characterization (Table S6) and RNA-seq profiling of the dorsolateral prefrontal cortex (De Jager et al., 2018). As in our *Drosophila* analyses, we first implemented CrypSplice, examining for cryptic splice errors among 241 controls versus 379 AD cases, based on AD consensus pathologic diagnostic criteria (see the STAR Methods). We identified few changes (n = 14) meeting our significance threshold (FDR < 0.05; Data S1, tab ix). In a complementary analysis focusing on 100 cases and 100 controls with high or low Tau pathologic burden, respectively, we identified a modestly increased number of cryptic splicing errors (n = 56) between the two groups (Data S1, tab x). Compared to our studies in *Drosophila* models, we reasoned that inter-individual heterogeneity may prevent detection of cryptic splicing events that recur among such a large number of samples. Moreover, if Tau-induced cryptic splicing errors occur stochastically and at low frequency, they may be distributed widely throughout the transcriptome, such that few recurrent errors might be detected among hundreds of samples. We therefore considered an alternative approach, deriving a person-specific “cryptic load” score, based on the average strength of cryptic junctions (see the STAR Methods). The cryptic load algorithm has been incorporated into our extended version of CrypSplice, enhancing this software tool for analysis of human RNA-seq datasets. Regression was first performed using consensus AD pathologic diagnosis as an outcome (379 cases and 241 controls), revealing a modest but non-significant increase in cryptic load in association with AD pathology ($\beta = 1.7$, $p = 0.09$; Table 1), after adjustment for age at death, postmortem interval (PMI), and sample batch. To improve our statistical power to detect Tau-associated cryptic splicing errors, we next considered an alternative strategy in which a subset of subjects was dichotomized into high (n = 136) versus low (n = 105) neurofibrillary tangles, based on Braak staging consensus criteria (Braak and Braak, 1991). We observed a significant association between Tau and cryptic load ($\beta = 2.6$, $p = 0.01$). Lastly, we employed a quantitative measure of neurofibrillary tangle burden as the outcome and performed a sensitivity analysis, in which subjects were selected from each tail of the distribution (i.e., high versus low tangle burden) and examined for differences in cryptic load. Consistent with our hypothesis, we found an increased estimate effect size and significant associations between Tau pathologic burden and cryptic load for more extreme comparisons among nested case and control groups considering total sample sizes from 600 down to 100 brains ($0.004 < p < 0.1$) (Table 1; Figure S7C). In sum, our data support a conserved relationship between Tau pathologic burden and cryptic splicing errors in human brains.

DISCUSSION

Integrating data from human brain autopsies and *Drosophila* models, we discover an unexpected mechanism of Tau-mediated neurodegeneration in AD converging on mRNA splicing. First, we show that numerous spliceosome components are physically associated with Tau in human brains with AD pathology, and in *Drosophila*, genetic manipulation of these factors enhances Tau neurotoxicity. Second, we find that transgenic expression of human Tau causes a reduction of multiple spliceosome components, and loss of function of the core spliceosome protein, *SmB*, is sufficient to induce progressive neuronal dysfunction and loss independent of Tau. Lastly, we show that Tau induces splicing errors in *Drosophila*

similar to genetic disruption of the spliceosome, and we confirm an increased cryptic splicing load in human postmortem brains with Tau pathology. Overall, our data support a model (Figure 6) whereby Tau-spliceosome interactions disrupt snRNP function, leading to splicing errors, loss of transcriptome fidelity, and ultimately neurodegeneration.

The Spliceosome, Transcriptome Integrity, and Maintenance of the Nervous System

In humans, dominantly inherited mutations in *SNRPB* cause cerebro-costo-mandibular syndrome, a rare developmental disorder (Lynch et al., 2014). The *SNRPB* paralog, *SNRPN*, which is specifically expressed in the nervous system, is found at the imprinted, Prader-Willi syndrome locus, and altered expression may contribute to neurodevelopmental delay (Cassidy et al., 2012). Given the essential role of splicing, nearly all mutations previously recovered in core spliceosome proteins, including *SmB*, are embryonic lethal in *Drosophila* and other models. Our serendipitous discovery of a viable, hypomorphic allele of *SmB*, encoding a ubiquitously expressed, core component of the spliceosome, facilitates study of the fundamental cellular splicing machinery in the maintenance and function of the adult nervous system. The brain appeared to be normally developed in *SmB* mutant adults; however, in aged animals we documented neuronal loss, progressive locomotor impairment, and decreased survival. These defects were rescued by neuronal-specific expression of wild-type *SmB.* Therefore, the *Drosophila* nervous system is especially vulnerable to reduction in spliceosome function, and susceptibility for resulting neurodegeneration increases with aging. Splicing is a major driver of transcriptome diversity, and in both *Drosophila* and mammals, alternative splicing is highest in the brain compared with all other tissues, consistent with an important role for the splicing machinery in neuronal diversity and brain health (Li et al., 2007; Raj and Blencowe, 2015). While additional studies will be required to confirm the mechanisms, it is likely that degradation of transcriptome fidelity in *SmB* mutant flies directly results in progressive neuronal dysfunction and death. RNA-seq profiles reveal that *SmB* loss of function causes massively dysregulated splicing, including thousands of differentially expressed splice forms and hundreds of splicing errors, including intron retention and cryptic junctions. These data are consistent with prior reports of genetic manipulation of spliceosome components in mouse models, in which aberrant pre-mRNA splicing is accompanied by neurodegeneration. For example, loss of either the *U2 snRNA* or *RBM17* induced cryptic splice junctions and intron retention, along with prominent cerebellar degeneration (Jia et al., 2012; Tan et al., 2016).

Splicing Errors and Transcriptome Fidelity in AD

Spliceosome disruption and altered pre-mRNA processing are also implicated in the pathogenesis of human diseases, including hematologic cancers (Hsu et al., 2015; Yoshida et al., 2011) and multiple neurologic disorders (Cooper et al., 2009). Mutation of *SMN*, encoding an essential cofactor for snRNP biogenesis, causes the recessive neurodegenerative disease spinal muscular atrophy (Lefebvre et al., 1995; Lorson et al., 1999). More recently, genetic variants affecting numerous RNA-binding protein splicing factors have been identified in familial FTD-ALS (Ito et al., 2017), and most of these proteins, including TDP-43, FUS, TAF15, TIA1, and hnRNPA2B1, closely associate with the spliceosome complex (Förch et al., 2002; Freibaum et al., 2010; Leichter et al., 2011; Martinez et al., 2016; Sun et al., 2015).

In the *Drosophila* nervous system, Tau induced a similar profile of splicing errors as *SmB* loss of function, and genetic manipulation of numerous core snRNP components enhanced Tau toxicity. Many of the same genes were vulnerable to splicing errors in Tau transgenics and *SmB* mutants. Further, we found that the splice donor and acceptor sites most susceptible to errors had weaker binding sites for the U1 and U2 snRNPs, respectively. Mutant forms of Tau causing accelerated neurodegenerative phenotypes in both humans and flies also showed more profound transcriptome disruption, and cryptic splicing errors were more frequent in aged animals. Together, these data strongly suggest that spliceosome disruption and resulting splicing errors may mediate Tau-induced neurotoxicity in AD and other tauopathies. Compared to studies of FTD-ALS (Humphrey et al., 2017; Ling et al., 2015; Polymenidou et al., 2011; Tan et al., 2016), altered splicing has only recently been systematically investigated in AD. Raj et al. (2018) reported on global splicing changes associated with human cortical Tau pathologic burden, including hundreds of potential intron retention events. Consistent with our findings in *Drosophila* models, *MAPT* expression in human neuronal cultures was sufficient to trigger splicing errors. Using the same ROSMAP brain autopsy sample, we now extend these findings to demonstrate evidence of cryptic splicing errors in human tissue with AD pathology. This class of error was previously described in FTD-ALS (Humphrey et al., 2017; Ling et al., 2015; Tan et al., 2016). The extended CrypSplice tool used for our study focuses exclusively on non-annotated junctions. Therefore, many of the Tau-associated changes that we highlight likely represent bona fide splicing errors, consistent with our hypothesis that Tau may disrupt the fundamental splicing machinery. Nevertheless, while CrypSplice readily identified substantial numbers of cryptic junctions from *Drosophila* heads, comparatively few such recurrent errors were discovered from human brains, instead requiring consideration of the global cryptic load. Inter-individual heterogeneity (i.e., human brains) and cellular heterogeneity (i.e., bulk tissue from human brains or fly heads) may limit assay sensitivity. Rapid improvements in RNA-seq methods, including single-cell approaches, along with further refinement in bioinformatic tools, will likely allow for even more robust detection and analysis of splicing errors in the future.

We argue that splicing errors are likely a cause rather than a consequence of Tau-induced neurotoxicity. First, splicing changes were detectable in young flies, preceding the onset of neurodegeneration (Wittmann et al., 2001). Second, direct manipulation of a core spliceosome component, *SmB*, also causes neurodegeneration in *Drosophila*. Third, RNAi knockdown of five different spliceosome components, including both core (*SmB, SmD2*, and *SmE*) and U1-specific factors (*U1C* and *snRNP-U1–70K*) enhanced Tau retinal toxicity. Moreover, we found dose-dependent, haploinsufficient genetic interactions with Tau for both *SmB* and *U1A* in the eye (electroretinogram), and for both *SmB* and *snRNP-U1–70K* in the brain (vacuolar degeneration). Contextual differences in the observed interactions might be explained by either variation in Tau sensitivity between tissues and/or the differential expression of specific spliceosome factors. Broadly, we propose two mechanistic models for how splicing errors and resulting transcriptome perturbation may promote neurodegeneration in AD. First, global degradation in transcriptome fidelity may overwhelm cellular RNA and/or protein quality control mechanisms (Garneau et al., 2007; Pilla et al., 2017). Accumulation of non-productive transcripts might be directly cytotoxic, and

translation could also lead to misfolded, dysfunctional proteins, and resulting proteostatic stress. Our recent study of AD postmortem brain tissue identified “cryptic peptides” corresponding to many mRNA splicing alterations, including those creating new exonic splice junctions (Johnson et al., 2018). Alternatively, selected cellular pathways essential to neuronal health and/or survival may be particularly vulnerable to splicing errors. In fact, Tau-associated splicing errors were significantly enriched in genes implicated in synaptic function and immune response, which are each strongly implicated in AD pathogenesis (Heppner et al., 2015; Spires-Jones and Hyman, 2014), and similar processes were impacted by cryptic splicing errors in TDP-43 cellular and mouse models relevant to FTD-ALS (Polymenidou et al., 2011). These two models are not mutually exclusive, and Tau-induced transcriptomic changes may promote a global cellular stress response, while simultaneously targeting specific cellular pathways that hasten the demise of neurons.

Tau-Spliceosome Interactions in AD

Additional work will be required to define the precise mechanism(s) by which Tau disrupts the spliceosome, but our findings and other published evidence provide important clues. One possibility is that insoluble Tau coaggregates with and sequesters spliceosomal factors in the cytoplasm (Figure 6, right). In prior work, multiple core and specific components of the U1 snRNP were abnormally enriched with misfolded and aggregated Tau in insoluble protein fractions from AD postmortem brain, and these proteins closely associated with Tau in neurofibrillary tangles (Bai et al., 2013; Bishof et al., 2018; Hales et al., 2014; Johnson et al., 2018). However, abundant evidence suggests that Tau neurotoxicity may be mediated by predominantly oligomeric, soluble forms (Cowan and Mudher, 2013). Additionally, while Tau and spliceosomal factors co-aggregated in *Drosophila* glia, the sequestration model cannot easily account for all of our findings since Tau does not form substantial insoluble aggregates in fly neurons (Wittmann et al., 2001). We therefore hypothesize that soluble forms of Tau may also interact with and disrupt the assembly and/or stability of the spliceosome (Figure 6, left). Consistent with this, we discovered that Tau coimmunoprecipitates with spliceosomal proteins in soluble fractions from AD postmortem brain homogenates. Interestingly, in a mouse model of tauopathy, numerous RNA-binding proteins colocalized with diffuse and oligomeric forms of Tau, but were excluded from more mature, fibrillar aggregates (Maziuk et al., 2018). Tau, along with many RNA-binding proteins, have intrinsically disordered structures and are capable of liquid-liquid phase separation (Ambadipudi et al., 2017; Bishof et al., 2018; Kim et al., 2013; Lee et al., 2016a; Molliex et al., 2015; Patel et al., 2015; Wegmann et al., 2018). Such interactions facilitate the assembly of membrane-less organelles with critical roles in RNA processing, such as cytoplasmic RNA stress granules and nuclear speckles, that regulate translation and splicing, respectively (Hyman et al., 2014; Lin et al., 2015; Nott et al., 2015). However, pathologic fibrillation of disease-associated proteins can perturb cellular dynamics of liquid-liquid phase separation with deleterious functional consequences (Lee et al., 2016a; Patel et al., 2015). For example, interactions between Tau and RNA-binding proteins, including ribosomal proteins and RNA stress granule components, can disrupt translation (Meier et al., 2016). Repeat expansion in *C9ORF72*, the most common cause of FTD-ALS, triggers accumulation of cytotoxic dipeptide repeats that avidly bind U2 snRNP components and disrupt spliceosome assembly (Yin et al., 2017). In mammalian cells, failure to assemble the

snRNP core leads to rapid lysosomal degradation of Sm proteins (Prusty et al., 2017). Other studies also support the existence of regulatory feedback loops that both preserve cellular spliceosome levels and component stoichiometry. For example, gene expression of spliceosome components can either be auto-regulated through non-productive splicing and/or RNA turnover (van Gelder et al., 1993; Gunderson et al., 1994; Lynch et al., 2014; Saltzman et al., 2011). We found that Tau induced a ~30%−50% reduction in multiple core and U1-specific spliceosomal proteins in *Drosophila* brains. In the case of SmB, SmD3, and U1A, stable mRNA levels support a post-transcriptional, and possibly, a post-translational mechanism. By contrast, for U1–70K (also reduced) and SmD2 (paradoxically increased), we speculate that compensatory, feedback mechanisms may be responsible for altered mRNA expression. Tau has also recently been demonstrated to disrupt nuclear pore integrity and function (Eftekharzadeh et al., 2018). Therefore, altered production, assembly, turnover, and/or nucleocytoplasmic transport of snRNPs might account for our findings.

The discovery of aberrant splicing in AD not only highlights an unexpected parallel with FTD-ALS, but may also support a mechanistic connection between neurodegeneration and carcinogenesis (Majd et al., 2019). Global splicing errors have been documented in diverse neoplasms (Dvinge and Bradley, 2015), and somatic, gain-of-function mutations in spliceosome components promote hematologic malignancies (Hsu et al., 2015; Yoshida et al., 2011). These observations have stimulated interest in pharmacologic strategies for modulating splicing (DeNicola and Tang, 2019; Lee et al., 2016b). However, as suggested by our genetic manipulations of *SmB*, it is likely easier to disrupt spliceosome function by targeting a single, critical component rather than restoring splicing, which may require simultaneous manipulation of many components. Our results nevertheless implicate defective spliceosomal biogenesis and function, along with resulting transcriptome perturbations, as a contributor to Tau-mediated neurodegeneration in AD, potentially amenable to therapies.

STAR★METHODS

LEAD CONTACT AND MATERIALS AVAILABILITY

Further information and requests for resources and reagents should be directed to and will be fulfilled by the Lead Contact, Joshua M. Shulman (joshua.shulman@bcm.edu). All *Drosophila* strains generated for this study are available on request without restriction. No other unique reagents were generated in this study.

EXPERIMENTAL MODEL AND SUBJECT DETAILS

Human Subjects—The Religious Orders Study and Rush Memory and Aging Project (ROSMAP) participants were free of known dementia at enrollment, agreed to annual clinical evaluations, and signed an informed consent and Anatomic Gift Act donating their brains at death, approved by the Institutional Review Board at Rush University (Bennett et al., 2018). AD clinical diagnoses were made following National Institute of Neurological and Communicative Disorders and Stroke-Alzheimer's Disease and Related Disorders Association recommendations (McKhann et al., 1984). Modified Bielschowsky silver stain was used to visualize neuritic plaques, diffuse plaques, and neurofibrillary tangles in tissue

sections from the midfrontal, middle temporal, inferior parietal, and entorhinal cortices and the hippocampal CA1 sector (Bennett et al., 2006). AD neuropathologic diagnosis was made based on intermediate or high likelihood of AD by criteria from the National Institute on Aging and the Reagan Institute Working Group on Diagnostic Criteria for the Neuropathological Assessment of Alzheimer's Disease (National Institute on Aging, Reagan Institute Working Group on Diagnostic Criteria for the Neuropathological Assessment of Alzheimer's Disease, 1997). Subjects were also classified based on Braak staging consensus criteria (Braak and Braak, 1991), including high (5–6) and low (0–2) neurofibrillary tangle pathology scores. As in prior work (Bennett et al., 2009), a quantitative composite score for neurofibrillary tangle pathologic burden was created by dividing the raw counts in each region by the population standard deviation of the region-specific counts and then averaging the scaled counts over the 5 brain regions to create a single standardized summary measure. Clinical and demographic features of the ROSMAP decedents included in this study can be found in Table S6.

***Drosophila* Stocks—**Female flies were used for all experiments unless noted otherwise. Flies were raised and aged on molasses-based media at 25°C with ambient light. A comprehensive list of fly genotypes and strains used for all experiments is included in the Key Resources Table and Data S1, tab iii. For clarity, detailed experimental genotypes are noted in Figure legends or with the relevant assay methods, below. All *Drosophila* genetic experiments were controlled for potential genetic background effects, as detailed below, either relying on a common F1 heterozygous genetic background or outcrossed strains. UAS-SmB was generated by cloning *Drosophila* SmB cDNA downstream of the UAS promoter into pUAST-attB vector, which was then inserted using PhiC31 integrase into the attP2 site on 3L chromosome by embryo microinjection. SmB^{MG} was generated by GFP conversion of SmB^{MI} as described in Nagarkar-Jaiswal et al. (2015a). Briefly, female flies with the hs-FLP and vasa-phiC31 integrase on the X chromosome, and the FRT flanked GFSTF (EGFP-FlAsH-StrepII-TEVcs-3×Flag) cassette on the third chromosome were mated to SmB^{MI} males at 18°C. The resulting embryos were heat shocked at 37°C for 20 min in 3 consecutive days, and the adult progeny with desired genotype were selected and crossed with flies carrying *CyO* balancer, followed by PCR validation. For experiments characterizing $SmB^{MG/MG}$ animals (Figures 3, 4, and 5), we used the genotype $w^{1118}/yw; SmB^{MG/MG}$ generated from the following cross: $w^{1118}; SmB^{MG}/CyO \times yw; SmB^{MG}/CyO$. For control animals, we used flies of the genotype w^{1118}/yw. We also examined $SmB^{MG/MG}$ animals harboring a genomic rescue of the genotype $w^{1118}/yw; SmB^{MG/MG}; SmB^{GR}/+$ generated from the cross: $yw; SmB^{MG}/CyO \times w^{1118}; SmB^{MG}/CyO; SmB^{GR}/TM6B$. Therefore, experimental and control flies share a common F1 heterozygous background ($yw/+$).

METHOD DETAILS

Tau Immunoprecipitation and Human Postmortem Brain Proteomics—Healthy control (n = 4) and AD patient (n = 4) frontal cortex brain samples (Table S1) were homogenized in NP-40 lysis buffer (25 mM Tris-HCl at pH 7.5, 150 mM NaCl, 1 mM EDTA, 1% NP-40, 5% Glycerol, 5 mM iodoacetamide) with protease and phosphatase inhibitors using a bullet blender according to manufacturer's instructions followed by

centrifugation at 10,000 × *g* for 15 min at 4°C. Immunoprecipitation was performed as follows, normalizing to 1 mg of total protein from each sample per input: brain lysates were first pre-cleared using Protein A-Sepharose conjugated beads (Invitrogen). Lysates were incubated with 3 μg of anti-Tau monoclonal antibody (TAU-5) overnight at 4°C. Purified Mouse IgG2a K isotype (BD PharMingen) was used as an isotype-matched negative control. 50 μL of Protein G DynaBeads (Invitrogen) beads were incubated with the lysate for 1 hr. Beads were then washed 3 times using wash buffer (50 mM Tris HCl at pH 8.0, 150 mM NaCl and 1% NP-40) and rinsed three times using phosphate buffered saline (PBS). A portion of the Dynabeads was subjected to western blot analysis (below) (Figure 1A).

The remaining beads were rinsed in PBS (3X) and re-suspended in 500 μL 50 mM NH_4HCO_3. Proteins bound to beads were reduced using 1 mM dithiothreitol (DTT) for 30 min and alkylated with 5 mM iodoacetamide (IAA) for 30 min in darkness. Proteins were digested with 1:100 (w/w) lys-C endopeptidase (Wako) at room temperature for 3 hr followed by further overnight digestion with 1:50 (w/w) trypsin (Promega) at RT. Tryptic peptides were acidified using 1% formic acid and 0.1% trifluoroacetic acid before desalting and purification using C18 StageTip. Peptides were eluted in 50% acetonitrile and were dried using a SpeedVac (Savant). Dried peptides were reconstituted in peptide loading buffer (0.1% formic acid, 0.03% trifluoroacetic acid, 1% acetonitrile). Peptide mixtures were separated by liquid chromatography on a self-packed C18 (1.9 um Dr. Maisch, Germany) fused silica column (25 cm × 75 μm internal diameter; New Objective, Woburn, MA) by a NanoAcquity UHPLC (Waters, Milford, FA) and monitored on a Q-Exactive Plus mass spectrometer (ThermoFisher Scientific, San Jose, CA). Elution was performed over a ~120-minute gradient at a rate of 400 nL/min with buffer B ranging from 3% to 80% (buffer A: 0.1% formic acid and 5% DMSO in water, buffer B: 0.1% formic and 5% DMSO in acetonitrile). The mass spectrometer cycle was programmed to collect one full MS scan followed by 10 data dependent tandem mass spectrometry MS/MS scans. The MS scans (300–1800 m/z range, 1,000,000 AGC, 150 ms maximum ion time) were collected at a resolution of 70,000 at m/z 200 in profile mode and the MS/MS spectra (2 m/z isolation width, 25% collision energy, 100,000 AGC target, 50 ms maximum ion time) were acquired at a resolution of 17,500 at m/z 200. Dynamic exclusion was set to exclude previous sequenced precursor ions for 30 s within a 10-ppm window. Precursor ions with +1, and +6 or higher charge states were excluded from sequencing.

The MaxQuant (Cox et al., 2014; Luber et al., 2010) (v1.5.5.1) LFQ algorithm was used for protein quantitation as previously described (Seyfried et al., 2017). UniProt protein sequences containing both Swiss-Prot and TrEMBL human protein sequences (90,411 target sequences downloaded April 21, 2015), were duplicated into a reverted (decoy) peptide database, searched, and used to control peptide and razor protein false discovery rate (FDR) at 1% within MaxQuant. Methionine oxidation (+15.9949 Da), asparagine and glutamine deamidation (+0.9840 Da), N-terminal acetylation (+42.0106 Da) and cysteine carbamidomethylation (+57.0215 Da) were assigned as fixed modifications. Tryptic peptides with only 2 mis-cleavages were included in each database search. A precursor mass tolerance of ± 20 ppm was applied prior to mass accuracy calibration and ± 4.5 ppm after internal MaxQuant calibration. Other search settings included a maximum peptide mass of 6,000 Da, a minimum peptide length of 6 residues, 0.05 Da tolerance for high resolution

Orbitrap MS/MS scans, or 0.6 Da for low resolution MS/MS scans obtained in the linear ion trap. The FDR for peptide spectral matches, proteins, and site decoy fraction were all set to 1%. Following quantification, missing values were imputed assuming informative missingness such that missing values were replaced with a left Gaussian tail random distribution per parameters previously determined ideal for LFQ based studies (Tyanova et al., 2016). IgG (background) measurements were averaged if either or both AD and control non-specific IgG replicate measurements for summed intensity were non-missing. Otherwise, either non-missing measurement was used; in the case that both measurements were missing (low background), average noise level imputed value for the two IPs was used for background subtraction. Finally, background subtraction (possibly due to differential specificity of the non-specific IgG) was not allowed to produce final values below zero (i.e., negative values were set to zero).

Western Blot Analysis—For human samples, bound protein complexes were eluted by boiling in Laemmli sample buffer at 98°C for 5 min. Protein complexes were then resolved on Bolt 4%−12% Bis-Tris gels (Thermo Fisher Scientific) followed by transfer to nitrocellulose membrane using iBlot 2 dry blotting system (Thermo Fisher Scientific). Nitrocellulose membranes were incubated with blocking buffer for 30 min followed by overnight incubation using anti-Tau antibody (Tau-E178, Abcam). Membranes were washed with TBST wash buffer (Tris-buffered saline, 0.1% Tween 20) and incubated with fluorophore-conjugated AlexaFluor-680 or AlexaFluor-790 secondary antibodies (anti-mouse or anti-rabbit, 1:15000, Thermo Fisher Scientific) for 1 hr at room temperature. Membranes were washed three times with TBST and scanned using an Odyssey Infrared Imaging System (LI-COR Biosciences).

For *Drosophila*, protein lysates were prepared by homogenizing adult fly heads in 2X Laemmli Sample Buffer (Bio-Rad) (6 μL per head, 10 heads per sample) with a pestle mixer (Argos Technologies), followed by centrifugation at 21,300 x *g* at 4°C for 15 min. The supernatants were incubated at 95°C for 5 min before SDS-PAGE analysis. Proteins were separated by 10% Mini-Protein TGX Precast Protein Gels (Bio-Rad), transferred onto PVDF membrane (Millipore), blocked in 5% bovine serum albumin (Sigma) in Tris-buffered saline with 0.1% Tween-20 (Sigma), and immunoblotted using one of the following antibodies: mouse anti-Sm (Y-12, 1:100, Thermo Fisher Scientific), mouse anti-U1A (1:200, gift from Dr. Helen K. Salz), rabbit anti-SNRPD2 (1:250, Novus Biologicals), rabbit anti-U1–70K (1:1000), rabbit anti-Tau (1:5000, Dako), rabbit anti-GFP (1:1000, Invitrogen), rabbit anti-GAPDH (1:5000, GeneTex), mouse anti-Actin (1:1250, Millipore). Membranes were washed with TBST and incubated with HRP-conjugated secondary antibodies (anti-mouse or anti-rabbit 1:10000, Santa Cruz) for 2 hr at room temperature. Membranes were washed with TBST, detected using ECL (PerkinElmer), and scanned using ChemiDoc Imaging system (Bio-Rad). For analyses of spliceosome proteins in Tau flies (Figures 2A–2C), we examined *elav > Tau (elav-GAL4/+; +/+; UAS-Tau*^{R406W}*/+*) or controls (*elav-GAL4/+).* The *UAS-Tau*^{R406W} strain was backcrossed to w^{1118} flies for 5 generations, ensuring a shared, homogeneous genetic background for the experimental and control genotypes.

Sarkosyl Extraction—Methods for sarkosyl soluble/insoluble fractionation was adapted from Colodner and Feany, 2010. Briefly, 50 heads from 1- and 20-day-old control (*repo-GAL4, tub-GAL80^{TS}/+*) and glial Tau expressing (*repo-GAL4, tub-GAL80^{TS}, UAS-Tau^{WT}/+*) flies were homogenized in 50 μL of homogenization buffer (15 mM NaCl, 25 mM Tris-HCl at pH 7.4, 1 mM EGTA, 1 mM EDTA, and protease inhibitors) by a pestle mixer (Argos Technologies), followed by brief centrifugation to remove large debris. The homogenate was then centrifuged at 100,000 × *g* at 4°C for 1 hr. The resulting supernatant was saved as the soluble fraction, and the pellet was homogenized in salt/sucrose buffer (10% sucrose, 0.8 M NaCl, 10 mM Tris-HCl at pH 7.4, 1 mM EGTA, and protease inhibitors), followed by centrifugation at 15,000 × *g* at 4°C for 30 min. Sarkosyl was added to make 1% sarkosyl-containing supernatant, which was then incubated at 37°C for 1 hr, followed by centrifugation at 100,000 × *g* at 4°C for 2 hr. The resulting pellet was homogenized in 1% sarkosyl-containing salt/sucrose buffer again, followed by centrifugation at 100,000 × *g* at 4°C for 2 hr. Lastly, the resulting pellet was homogenized in 15 μL of homogenization buffer and then subjected to western blot analysis.

***Drosophila* Rough Eye Assay—**For analysis of genetic interactions using the rough eye assays (Figure 1B), photos of external eye appearance were acquired using a Leica EC3 system. Control genotypes included *GMR-GAL4/+* (Top Left) and *UAS-Tau^{V337M}/+; GMR-GAL4/+* (Bottom Left). Animals with expression of Tau + RNAi (Bottom row: *UAS-Tau^{V337M}/+; GMR-GAL4/UAS-RNAi* or *UAS-Tau^{V337M}/+; GMR-GAL4/+; UAS-RNAi/+*) were compared with RNAi expressed independently of Tau (Top row: *GMR-GAL4/UAS-RNAi* or *GMR-GAL4/+; UAS-RNAi/+).* RNAi lines tested include (left to right) *SmB^{HM05097}*, *SmD2^{v31947}*, *snRNP-U1–70K^{v23150}*, *snRNP-U1C^{v22132}*, and *SmE^{v23570}*. Additional RNAi strains were also tested but are not shown (Data S1, tab iii); consistent interactions were seen for *SmB^{v110713}*, *SmD2^{v31946}*, *SmD2^{HMC03839}*, *snRNP-U1–70K^{HMS00274}*, *snRNP-U1C^{v22133}*, *snRNP-U1C^{HMS00137}*, and *SmE^{HMS00074}*. All experimental and control genotypes shared a common F1 heterozygous background (*w^{1118}*/+; *GMR-GAL4/+)*, and we used control strain genotypes specific for each RNAi: (1) *w^{1118}*; (2) *y[1] v[1]; P{y[+t7.7] = CaryP}attP2;* or (3) *y[1] v[1]; P{y[+t7.7] = CaryP}attP40.* Quantification of rough eye phenotypes was performed as previously described (Shulman et al., 2014). Briefly, the size and roughness of eyes were scored using a 6-level rating scale: 0 (wild-type eye), 1 (very mild rough, < 50% facet disruption), 2 (mild rough, 50%−100% facet disruption, 0–25% reduction in eye size), 3 (moderate rough, 100% facet disruption, 25%−50% reduction in eye size), 4 (severe rough, additionally with one of the following features-ommatidial fusions, darkened/discolored areas, or > 50% reduction in eye size), 5 (very severe rough, two or more of the characteristic severe features are present).

Electrophysiology—Methods for electroretinogram (ERG) recordings were adapted from Chouhan et al. (2016). Briefly, 10 flies from each genotype in 1-, 5-, or 10-day-old were affixed to a glass slide. Flies were kept in the dark for at least 1 min prior to stimulation for 1-minute with alternating 2 s light/dark pulses. Retinal responses were recorded using electrodes placed on the corneal surface and the thorax (reference) and analyzed using LabChart software (ADInstruments). For analyses of ERG (Figure 1C), the following genotypes were examined: (1) *Rh1-GAL4/+;* (2) *Rh1-GAL4/SmB^{MG}*; (3) *Rh1-GAL4/+;*

UAS-Tau^{WT}/+; and (4) *Rh1-GAL4/SmB^{MG}*; *UAS-Tau^{WT}/+.* Experimental and control flies share a common F1 heterozygous background (*yw*/+; *Rh1-GAL4/+*).

Assays for *Drosophila* Survival and Climbing—For survival analyses, 288~337 flies per genotype were aged in the vials with less than 30 flies per vial. Surviving flies were counted and transferred to vials with fresh food every other day. For the startle-induced, negative geotaxis assay (climbing), 5–18 flies from each group were placed in an individual vial for a total of 5–7 vials for each group; sample/group size variability was due to reduced survival at aged time points. Flies from each vial were transferred to an empty vial without anesthetization prior to the assay. Locomotor activity was assessed by counting the number of flies climbing past the 5 cm line within a 5 s interval after gently tapping flies to the bottom of the vial. For initial characterization of *SmB^{MG}* survival and locomotor phenotypes, we examined the following genotypes (Figures 3D and 3E): (1, Ctrl-Gray) *w^{1118}/yw;* (2, Green) *SmB^{GR}/+;* (3, Blue) *SmB$^{MG/MG}$*; *SmB^{GR}/+);* and (4, Black) *SmB$^{MG/MG}$*. Experimental and control flies share a common F1 heterozygous background (*yw*/+ *or yw*/+; *SmB^{MG}/+).* For experiments testing rescue of *SmB^{MG}* survival and locomotor phenotypes by *elav* > *SmB*, the following genotypes were used (Figures 3F and 3G): (1, Yellow) *elav-GAL4/Y;* (2, Red) *elav-GAL4/Y;* +/+; *UAS-SmB/+;* (3, Black) *elav-GAL4/Y; SmB$^{MG/MG}$*; and (4, Blue) *elav-GAL4/Y; SmB$^{MG/MG}$*; *UAS-SmB/+.* Experimental and control flies share a common F1 heterozygous background (*w^{1118}*, *elav-GAL4/+*).

Histology and Immunofluorescence—For histology, *Drosophila* heads were fixed using 8% glutaraldehyde (Electron Microscopy Sciences) at 4°C for 6 days, followed by paraffin embedding and microtome sectioning, as previously described in Chouhan et al. (2016). Serial 5 μm-thick frontal sections (Leica) were prepared from *Drosophila* heads and mounted on slides, followed by hematoxylin and eosin staining or 3,3′-Diamino-benzidine (DAB) staining to examine brain morphology and cholinergic neurons, respectively. For *Drosophila* brain morphology, we quantified numbers of central brain vacuoles greater than 5 μm in diameter in 5 serial frontal sections at the level of the fan-shaped body. For analysis of Tau-SmB interactions (Figure 1D), the following genotypes were used: (1, Ctrl) *elav-GAL4/+;* (2) *elav-GAL4/+; SmB^{MG}/+;* (3) *elav-GAL4/+;* +/+; *UAS-Tau^{R406W}*/+; (4) *elav-GAL4/+; SmB^{MG}/+; UAS-Tau^{R406W}/+.* Experimental and control flies share a common F1 heterozygous background (*w^{1118}*, *elav-GAL4/+).* For analysis of neuron counts in *SmB^{MG}* brains (Figures 4A–4C), cortical nuclei were counted within a 6,400 μm^2 square area centered on the mushroom body calyx from well-oriented frontal sections. Experimental (*SmB$^{MG/MG}$*) and control flies (*w^{1118}/yw* or *SmB$^{MG/MG}$*; *SmB^{GR}/+*) share a common F1 heterozygous background (yw/+). For elav and repo staining (Figure S4F), frontal sections were incubated with anti-elav (1:20, DSHB) or anti-repo (1:30, DSHB) for 2 hr at room temperature following antigen retrieval and 1% normal horse serum blocking, and followed by secondary detection using (ABC) kit (Vector Laboratories) with DAB peroxidase substrate (Vector Laboratories) as described above. Fast Red was used for nuclei counterstain. For counting cholinergic neurons in *ChAT* > *lacZ* flies, frontal sections were incubated for 25 min in 10 mM sodium citrate at pH 6.0 at 98°C for antigen retrieval, followed by washing in phosphate-buffered saline (PBS) containing 0.3% Triton X-100 (PBST) for 5 min. After blocking in 1% normal horse serum in PBS for 20 min, sections

were incubated with anti-β-galactosidase antibody (1:250, Promega) for 1 hr at room temperature. Secondary detection was performed using the avidin-biotin-peroxidase complex (ABC) kit (Vector Laboratories) with DAB peroxidase substrate (Vector Laboratories) following the manufacturer's protocol. The number of immunoreactive neurons in the lamina within 60 μm area was counted as described previously in Wittmann et al., 2001. The following genotypes were examined (Figures 4D–4F): (1, Ctrl) *ChAT-GAL4/UAS-lacZ)*, (2) *ChAT-GAL4, SmB^{MG}/UAS-lacZ, SmB^{MG}*, (3) *ChAT-GAL4, SmB^{MG}/UAS-lacZ, SmB^{MG}; SmB^{GR}/+.* Experimental and control flies share a common F1 heterozygous background (*ChAT-GAL4/+).* All light microscopic images from histology and immunohistochemistry were acquired using a Leica DM 6000 B system.

For whole-mount immunofluorescence, *Drosophila* brains or imaginal discs were dissected and fixed using 4% formaldehyde in PBS at room temperature for 20 min, followed by washing with PBST twice for 10 min each, blocking with 5% normal goat serum in PBST for 1 h at room temperature. Brains were incubated with the primary antibodies at 4°C for 3 days, followed by incubation with secondary antibody and DAPI at 4°C for 24 hr. Third instar larval wing discs were incubated with the primary antibody at 4°C for 16 hr, followed by secondary antibody incubation for 2 hr at room temperature. Stained tissues were mounted with Vectashield mounting medium (Vector Laboratories). The following primary antibody dilutions were used: anti-Sm (Y-12, 1:1000 ~1:3000, Thermo Fisher Scientific), anti-U1A (1:1500, a gift from Dr. Helen K. Salz), anti-Tau[pS214] (1:200, Invitrogen). For secondary antibodies, we used Cy3-conjugated goat anti-mouse IgG (1:1000, Jackson ImmunoResearch) or Alexa Fluor 488-conjugated goat anti-rabbit IgG (1:1000, Jackson ImmunoResearch). Confocal microscopy images were acquired with a Leica SP8 confocal system (Leica Microsystems) and using Leica Application Suite X (LAS X) Software. For quantification of spliceosomal protein immunofluorescence (Figures 2D and 2E), intensity levels were measured and averaged within 314 μm^2 circular areas in the intersection of medial lobe of mushroom body, antennal lobe, and anterior ventrolateral protocerebrum and in between the antennal lobe and the prow. We examined *elav > Tau (elav-GAL4/+;* +/+; *UAS-Tau^{R406W}*/+) or controls (*elav-GAL4/+).* The *UAS-Tau^{R406W}* strain was backcrossed to *w^{1118}* flies for 5 generations, ensuring a shared, homogeneous genetic background for the experimental and control genotypes. Glial Tau and SmB co-aggregation (Figure 2F) was quantified in the optic lobes between medulla and lobula, in the following genotypes: control (*repo-GAL4, tub-GAL80^{TS}/+*) and *repo > Tau (repo-GAL4, tub-GAL80^{TS}, UAS-Tau^{WT}/+). Repo-GAL4, tub-GAL80^{TS}, UAS-Tau^{WT}/TM3* was maintained at 18°C to prevent Tau expression and Tau-mediated lethality. To induce glial Tau expression, flies of the indicated genotypes were shifted to 30°C on the day of eclosion. Experimental and control flies share a common F1 heterozygous background (*Canton-S*).

TUNEL Assay—TUNEL staining was performed using Click-iT Plus TUNEL Assay (Invitrogen). *Drosophila* brains were dissected and fixed by 4% formaldehyde in PBS at room temperature for 20 min, followed by washing with PBST twice for 10 min each, and Protease K treatment for 15 min at room temperature. After a brief wash with water for 5 min, brains were equilibrated in TdT reaction buffer at 37°C for 10 min, followed by incubation in TdT reaction mixture at 37°C for 70 min. After being washed with water and

PBST containing 5% normal goat serum for 5 min each, brains were incubated with Click-iT Plus TUNEL reaction cocktail at 37°C for 30 min. Brains were then washed by PBST containing 5% normal goat serum and water for 5 min each before mounted on slides with Vectashield DAPI-containing mounting medium (Vector Laboratories). Images were acquired using Z stack (5 μm per step) and TUNEL-positive signals central brain were counted at the level between ellipsoid body and fan-shaped body.

***Drosophila* RNA Sequencing—**For RNA-sequencing (RNA-seq) experimental design, we evaluated each of the following genotypes: (1) *elav > Tau^{WT}* (*elav-GAL4/+;* +/+; *UAS-Tau^{WT}/+* and *elav-GAL4/Y;* +/+; *UAS-Tau^{WT}/+);* (2) *elav > Tau^{R406W}* (*elav-GAL4/+;* +/+; *UAS-Tau^{R406W}/+* and *elav-GAL4/Y;* +/+; *UAS-Tau^{R406W}/+);* (3) *elav* control (*elav-GAL4/+* and *elav-GAL4/Y);* (4) *SmB (yw; SmB$^{MG/MG}$* and *yw/Y*; *SmB$^{MG/MG}$*); and (5) *yw* control (*yw* and *yw/Y).* For *elav > Tau* and *elav* controls, animals were evaluated at 1-, 10-, or 20-days. For *SmB* and *yw* controls, 10-day old animals were evaluated. To avoid possible batch effects, all experimental and control genotypes used for each comparison (*Tau^{WT}*, *Tau^{R406W}*, or *SmB*) were sequenced together. Triplicate samples, prepared from independent groups of pooled fly heads, were evaluated for all genotypes and age, except for the *elav* control genotype used for the comparison with *Tau^{R406W}*, for which duplicate samples were used:

Exp	Replicates (n)	Ctrl	Replicates (n)	Age (d)
Tau^{WT}	3	*elav*	3	1, 10, 20
Tau^{R406W}	3	*elav*	2	1,10, 20
SmB	3	*yw*	3	10

Total RNA was extracted from approximately 100 adult fly heads (for each genotype/age/sample), equally divided between males and females. Frozen fly heads were homogenized in Trizol (Invitrogen), treated with DNaseI (Promega), and total RNA was extracted using the RNeasy Micro Kit (QIAGEN). RNA-seq was performed following the Large Insert Strand Specific TruSeq protocol by the Genomics Platform at The Broad Institute. Each library was sequenced with 100 bp pair-end reads. Raw reads were obtained in binary format (BAM) format. Fastq files were extracted from bam files using Picard tools SamToFastq module. Sequencing quality and any adaptor contamination were assessed using FastQC v0.10 (Andrews, 2010). Average phred score for all samples was greater than 35. Average sequence depth for *Tau^{WT}*, *Tau^{R406W}*, and *SmB* samples (and respective controls) was 53M, 84M, and 79M read pairs, respectively. Due to reduced coverage, one of the *elav* control samples (10-day-old) from the *Tau^{WT}* comparison was re-sequenced and subsequently down sampled to 60M read pairs, using random selection in seqtk (https://github.com/lh3/seqtk). For the *SmB* comparison, one experimental and control sample were each down sampled to 90M read pairs. Based on the *Drosophila* transcriptome size (30M bp), average coverage across all samples is estimated at ~230X, which was deemed adequate for our subsequent splicing analysis pipeline. Raw reads were aligned to *Drosophila* reference genome dm6 and human reference genome GRCh38 and using STAR 2.5.3a (Dobin et al., 2013). Whole genome FASTA sequence and annotations of respective genome builds were downloaded from UCSC genome browser portal (http://hgdownload.soe.ucsc.edu/downloads.html). Raw

genome is indexed by setting-runMode to genomeGenerat in STAR. To reliably align splice junction, the raw reads were aligned to the indexed genome by setting an anchor length (splice junction) of 5 and-outSAMstrandField to intronMotif. Sample-wise alignments were saved as coordinate sorted BAM files. Average mappability of all samples was 96.5%. Gene level counts were obtained as the sum of total reads mapped to respective genes. As expected, based on principal component analysis using gene counts (Yalamanchili et al., 2017), sample clustering reflected genotype and age (Figure S8).

For the evaluation of differential expression of alternative splice forms we deployed rMATS (Shen et al., 2014). Alignment files (BAM) and reference annotations (GTF) from UCSC genome browser were passed to rMATS. Insert length is computed as average fragment size (400 bp) - (2*read length). rMATS classifies splicing events into 5 categories, skipped exons, retained introns, mutually exclusive exons, alternative 5′ ss, and alternative 3′ ss (Figure S6A). For analysis of intron retention, we developed and applied a new, complementary tool, Differential Expression of Introns (DEIn). In order to minimize false positive calls, either due to sequencing artifact, non-specific and/or multi-mapping, or incompletely processed mRNA, we required each intron to be fully covered (i.e., every nucleotide appears in at least 1 sequencing read) (see schematic in Figure S6B). Aligned RNA-seq (BAM) files were converted to bigwig format with a bin size of 2 using the bamCoverage module from deeptools (Ramírez et al., 2014). Based on the *Drosophila* reference genome dm6, we excluded all sequences that overlap with annotated exons. Coverage of each intron across all genotypes and time points were computed from respective bigwig files using bwtools (Pohl and Beato, 2014). Only fully covered introns in at least one of the samples were retained. Differential expression was determined using DESeq2 (Love et al., 2014), with fold-change > 0. In order to detect cryptic splicing errors, we used the published tool, CrypSplice (Tan et al., 2016). CrypSplice only considers splice junctions that have not previously been annotated in public databases; defining cryptic junction strength as the ratio of junction reads to total 5′ splice site coverage. For each cryptic junction, a strength difference is computed: experimental minus control samples. We focused on recurrent junction gains (junction strength difference > 0 and present in at least 2 samples per genotype examined) with a minimum threshold of at least 10 junction reads. Junctions spanning multiple genes were assigned to the gene of origin. In cases where cryptic junctions originate outside of a gene body, we computed the distance to the nearest gene and only considered junctions mapping within 500 bp of a gene. In order to prioritize candidate splicing errors for experimental validation, we focused on events that were significantly differentially expressed at all three time points evaluated. Second, we ranked all cryptic splicing errors and intron retention events based on their junction strength and fold change, respectively. Third, we manually examined each event using the Integrative Genomic Viewer and excluded events with either (i) low expression (< 20 RNA-seq read counts) or (ii) large/small predicted product size (> 10,000 or < 10 base pairs), which were deemed infeasible for validation by RT-PCR. Based on these criteria, 13 splicing errors were selected for validation, including 7 cryptic splice junctions and 6 intron retention events. Oligonucleotide primers for PCR-validation of selected splicing errors are included in Data S1, tab xi.

For descriptive purposes, CrypSplice was enhanced to assign cryptic junction categories (Figure 5A), including new splice donor (D), new splice acceptor (A), N (new splice donor

and new splice acceptor), NDA (exon skipping). All genes with splicing errors identified by DEIn (intron retention) CrypSplice (cryptic junctions) were further annotated based on numbers of introns and alternative transcript splice forms. The positions of splicing errors within transcripts were annotated with respect to coding regions, 5′ untranslated regions (UTRs), and 3′ UTRs. For characterization of Tau/SmB overlaps and gene features (Figures 5D, 5E, and 5G), we examined the union of all cryptic splice and intron retention events detected in Tau^{R406W} flies at the 1-, 10-, and 30-day time points. We also examined the consensus sequences for error-prone splice donor and acceptor sequences (Figures 5F and S7B), including splice sites flanking all retained introns (DEIn) and those splice sites "skipped" to generate cryptic splice donor or acceptors (CrypSplice). In the case of cryptic splicing errors, we inferred the "original" annotated splice donor and/or acceptor site that likely contributed to the generation of cryptic junction. As diagrammed in Figure S7A, due to alternative transcript isoforms arising from many genes, it is only possible to systematically infer these sites with high confidence in the case of the cryptic splicing errors that generate either new splice donor or acceptor sites. In this situation, the corresponding preserved splice donor/acceptor site serves as an anchor for our split RNA-seq reads, allowing unambiguous mapping to the specific isoform and subsequent determination of the error-prone splice donor or acceptor site. Alternatively, in the case of errors involving both new splice acceptor and donor sites (or exon-skipping events), it is not always possible to confidently infer the error-prone splice site. The binding strength of splice donor and acceptor sites was determined based on the entropy of respective 5′ (−3 bp exonic to +6 bp intronic) and 3′ (−20 bp intronic to +3 bp exonic) splice site sequences (Yeo and Burge, 2004).

Human (ROSMAP) RNA-seq Analysis—For CrypSplice analysis of ROSMAP RNA-seq data, we initially dichotomized based on AD pathologic diagnosis (above). In a complementary approach, we also compared 100 cases and 100 controls selected from the extremes (high/low) of neurofibrillary tangle pathology, using the quantitative composite score for tangle pathologic burden (see also below). Our analyses focused on junction gains (junction strength difference > 0) with a minimum threshold of at least 5 reads and detected in greater than 50% of cases and less than 50% of controls. In order to evaluate non-recurrent cryptic splicing errors, we developed and applied the Cryptic Load tool. Cryptic Load computes a person-specific cryptic splicing burden, based on average cryptic junction strength,

$$CL(S) = \frac{\sum_{j=1}^{n} \frac{JC_j}{EC_j}}{n}$$

where, $CL(S)$ is the Cryptic Load of a sample S, JC_j is the read count of junction j, EC_j is the respective 5′ exon coverage of junction j, and n is the total number of cryptic junctions in sample S. Cryptic load was further normalized to respective sequencing depth. For initial alignment and mapping of junctions from a large number of ROSMAP samples, we used the cloud formation cluster at Amazon Web Services. We created one EC2 master instance (m3.xlarge) which was used to launch EC2 computing nodes of type (c3.8xlarge).

Quantitative Real-Time PCR (qRT-PCR)—Total RNA was prepared from *Drosophila* heads as described above. Following reverse transcription using the SuperScript III First-Strand Synthesis System (Invitrogen), qRT-PCR was performed using iQ SYBR Green Supermix (Bio-Rad) in a CFX96 Touch Real-Time PCR Detection System (Bio-Rad) with standard cycling parameters. Each reaction was performed in triplicate. *RpL32* was used as an endogenous control for normalization of each transposon to calculate ΔCt values. Primers used are listed in Data S1, tab xi.

QUANTIFICATION AND STATISTICAL ANALYSIS

Human Tau IP LC-MS/MS Analyses—Differentially enriched or depleted proteins in the Tau interactome were determined by calculating t test p values (unpaired) and fold change difference (±1.5 fold) for the pairwise comparison of AD versus control, using the aov() and anova() functions in R. The ANOVA p value (probability > F) calculation provides identical results to t.test() when only 2 groups are compared. Volcano plots were generated with the R ggplot2 package. 'Spliceosome', 'RNA metabolism', and 'Translation', GO-associated genes were downloaded on 11/16/2018 from geneontology.org, and matching gene symbols in the IPs were annotated in Data S1, tab i. DAVID v6.8 was used to calculate enrichment p values for gene ontologies enriched among the Tau-associated proteins differentially increased in AD (fold change ≥ 1.5 and p value < 0.05). A background list of gene symbols was generated from the proteomic analysis of the input total brain homogenate prepared from the same brain autopsy cases, as previously described (Abreha et al., 2018). In total, 4,239 unique gene products made up this background reference proteome. Next, STRING (Snel et al., 2000) was used to map functional interactions among the increased AD Tau interacting proteins assigned to the "Poly(A)-RNA binding," "Translation" or "Ribonucleoprotein" GO-terms (n = 105 total). Proteins from the "Ribonucleoprotein" cluster in STRING (Figure S1C) were clustered hierarchically using the NMF package aheatmap function, with euclidian distance and complete linkage, and summed intensity data were converted to fold standard deviation (SD) from the mean for each row (i.e., Z score) prior to clustering.

Drosophila* Experimental Data Analyses—Drosophila* experimental image data were analyzed using ImageJ (NIH). The sample size for all comparisons is included in each Figure legend. Statistical analyses used either two-tailed, unpaired t tests or Analysis of Variance (ANOVA), followed by Tukey's post hoc test for multiple comparisons. Survival assays were analyzed using the Kruskal-Wallis test, followed by Dunn's test for post hoc comparisons. The significance threshold for all analyses was set to $p < 0.05$ and is noted in figures using the following convention: *, $p < 0.05$; **, $p < 0.01$; ***, $p < 0.001$. Otherwise, results are noted at "not significant" (ns). Error bars in all analyses represent the standard error of the mean (SEM). Sample sizes for all analyses are indicated in Figure legends, referring to the number of animals examined, or replicate studies performed.

For statistical comparisons of *Drosophila* RNA-seq results, the default tests were used as implemented within rMATS (likelihood ratio test), DEIn/DESeq2 (Wald test), and CrypSplice (beta-binomial test). The significance threshold was set to adjusted p value (FDR) < 0.05, based on the Benjamini-Hochberg procedure. For the analyses of Tau/SmB

overlaps and gene features (Figures 5D, 5E, and 5G), we examined the union of all cryptic splice and intron retention events detected in Tau^{R406W} flies at the 1-, 10-, and 30-day time points. For the analysis of U1 (5′-splice site) and U2 (3′-splice site) consensus sequences contributing to cryptic splicing errors (Figures 5F, S7A, and S7B), we considered all splicing errors that generate either new splice donor or acceptor sites (union of 1-, 10-, and 20-day time points) (see also related Methods above). For analyses of gene/transcript/junction features, including intron or alternative splice form numbers (Figure 5E) and 5′/3′ splice site binding strength scores (Figure S7B), random sampling was implemented to determine an empirical p value using python. Random samples were drawn from the background of all *Drosophila* genes/transcripts/exon-intron junctions, respectively, using a gene set size equal to the experimentally determined comparison group (e.g., n = 592 genes for Tau-associated cryptic splicing errors). P value was computed based on 1000 random samples, noting the frequency of mean feature values as or more extreme than the experimental set. Gene sets with Tau-associated splicing errors were evaluated for functional enrichment of biological process (BP) gene ontology terms using DAVID 6.8 (Huang da et al., 2009a, 2009b) with a standard *Drosophila melanogaster* background. Data S1, tab viii, displays all results meeting a significance threshold of $p < 0.001$, and overlapping genes, $n > 5$. For determining the overlap of cryptic splicing errors between Tau^{R406W} and *SmB* flies, we considered (1) all unique junctions, or alternatively, "nested" junctions affecting either (2) the same exon/intron or (3) gene. The hypergeometric test was performed with a stringent background set in each case. For junctions (1), the background consists of recurrent cryptic junction gains present in at least 2 samples per genotype examined with a minimum threshold of at least 10 junction reads (n = 11,904). We next collapsed the background cryptic junctions affecting either a common exon or intron to determine the splicing error background per-exon/intron (2) (n = 7,039). Lastly, for the per-gene analysis, the background consisted of all *Drosophila* genes (n = 12,705). For intron retention events, we similarly examined overlaps based on (2) per-intron or (3) per-gene criteria.

ROSMAP RNA-seq Analysis—As described above for *Drosophila*, CrypSplice analyses of ROSMAP RNA-seq data also used the beta-binomial test and a significance threshold of FDR < 0.05. For analyses of CrypticLoad, linear regression was performed using the model,

$$Cryptic\ Load \sim X + Batch + PMI + Age$$

where X = case/control, and additional covariates were included for sequencing batch, postmortem interval (PMI) and age of death (Age). Case / Control status was assigned using 3 separate outcome traits: AD pathologic diagnosis, Braak neurofibrillary tangle stage (high/low), or quantitative neurofibrillary tangle pathologic burden. For tangle burden, we selected equal numbers of cases and controls from each tail of the distribution (high versus low tangle burden) varying total sample size (cases + controls) between 600 and 100 brains (Table 1). For data visualization, cumulative density plots were generated using the ecdf() function and ggplot2 R, stratifying based on AD diagnosis, Braak tangle stage, or neurofibrillary tangle burden.

DATA AND CODE AVAILABILITY

RNA-seq data from *Drosophila* and human postmortem samples (ROSMAP) are available on the AMP-AD Knowledge Portal (https://www.synapse.org/ampad) (https://doi.org/10.7303/syn2580853). ROSMAP clinicopathologic data is available for request from the RADC Research Resource Sharing Hub (www.radc.rush.edu). Scripts and analysis pipelines used in this study, including CrypSplice, CrypticLoad, and DEIn, are available at: www.liuzlab.org/Scripts_Tau-SmB.zip.

Supplementary Material

Refer to Web version on PubMed Central for supplementary material.

ACKNOWLEDGMENTS

We thank H.J. Bellen, J. Botas, M.B. Feany, A.G. Matera, and H.K. Salz for providing antibodies and *Drosophila* stocks. We thank the Bloomington *Drosophila* Stock Center, the Vienna Drosophila RNAi Center, FlyBase (Gramates et al., 2017), and Biorender.com. This study was supported by grants from the NIH (R01AG053960, R01AG036836, R01AG050631, R01AG057339, U01AG046161, P30AG10161, R01AG15819, R01AG17917, U01AG46152, R01GM120033, U01AG061357, P30CA125123, and U54HD083092). J.M.S. was additionally supported by the Huffington Foundation, the Jan and Dan Duncan Neurological Research Institute at Texas Children's Hospital, and a Career Award for Medical Scientists from the Burroughs Wellcome Fund. Z.L. received support from the Cancer Prevention Research Institute of Texas (RP170387), the Houston Endowment, and the Belfer Neurodegenerative Disease Consortium. We thank Drs. Hugo Bellen, Hamed Jafar-Nejad, Herman Dierick, Hui Zheng, Joanna Jankowsky, Thomas Westbrook, Thomas Cooper, and Juan Botas for feedback and discussions.

REFERENCES

Abreha MH, Dammer EB, Ping L, Zhang T, Duong DM, Gearing M, Lah JJ, Levey AI, and Seyfried NT (2018). Quantitative Analysis of the Brain Ubiquitylome in Alzheimer's Disease. Proteomics 18, e1800108. [PubMed: 30230243]

Ali YO, Ruan K, and Zhai RG (2012). NMNAT suppresses tau-induced neurodegeneration by promoting clearance of hyperphosphorylated tau oligomers in a Drosophila model of tauopathy. Hum. Mol. Genet 21, 237–250. [PubMed: 21965302]

Ambadipudi S, Biernat J, Riedel D, Mandelkow E, and Zweckstetter M (2017). Liquid-liquid phase separation of the microtubule-binding repeats of the Alzheimer-related protein Tau. Nat. Commun 8, 275. [PubMed: 28819146]

Andrews S (2010). FastQC: a quality control tool for high throughput sequence data.http://www.bioinformatics.babraham.ac.uk/projects/fastqc.

Anne J (2010). Arginine methylation of SmB is required for Drosophila germ cell development. Development 137, 2819–2828. [PubMed: 20659974]

Arriagada PV, Growdon JH, Hedley-Whyte ET, and Hyman BT (1992). Neurofibrillary tangles but not senile plaques parallel duration and severity of Alzheimer's disease. Neurology 42, 631–639. [PubMed: 1549228]

Bai B, Hales CM, Chen P-C, Gozal Y, Dammer EB, Fritz JJ, Wang X, Xia Q, Duong DM, Street C, et al. (2013). U1 small nuclear ribonucleoprotein complex and RNA splicing alterations in Alzheimer's disease. Proc. Natl. Acad. Sci. USA 110, 16562–16567. [PubMed: 24023061]

Bardai FH, Wang L, Mutreja Y, Yenjerla M, Gamblin TC, and Feany MB (2018). A conserved cytoskeletal signaling cascade mediates neurotoxicity of FTDP-17 tau mutations in vivo. J. Neurosci 38, 108–119. [PubMed: 29138281]

Bennett DA, Schneider JA, Tang Y, Arnold SE, and Wilson RS (2006). The effect of social networks on the relation between Alzheimer's disease pathology and level of cognitive function in old people: a longitudinal cohort study. Lancet Neurol. 5, 406–412. [PubMed: 16632311]

Bennett DA, De Jager PL, Leurgans SE, and Schneider JA (2009). Neuropathologic intermediate phenotypes enhance association to Alzheimer susceptibility alleles. Neurology 72, 1495–1503. [PubMed: 19398704]

Bennett DA, Buchman AS, Boyle PA, Barnes LL, Wilson RS, and Schneider JA (2018). Religious Orders Study and Rush Memory and Aging Project. J. Alzheimers Dis 64 (s1), S161–S189. [PubMed: 29865057]

Bishof I, Dammer EB, Duong DM, Kundinger SR, Gearing M, Lah JJ, Levey AI, and Seyfried NT (2018). RNA-binding proteins with basic-acidic dipeptide (BAD) domains self-assemble and aggregate in Alzheimer's disease. J. Biol. Chem 293, 11047–11066. [PubMed: 29802200]

Braak H, and Braak E (1991). Neuropathological stageing of Alzheimer-related changes. Acta Neuropathol. 82, 239–259. [PubMed: 1759558]

Brahms H, Raymackers J, Union A, de Keyser F, Meheus L, and Lührmann R (2000). The C-terminal RG dipeptide repeats of the spliceosomal Sm proteins D1 and D3 contain symmetrical dimethylarginines, which form a major B-cell epitope for anti-Sm autoantibodies. J. Biol. Chem 275, 17122–17129. [PubMed: 10747894]

Cassidy SB, Schwartz S, Miller JL, and Driscoll DJ (2012). Prader-Willi syndrome. Genet. Med 14, 10–26. [PubMed: 22237428]

Chouhan AK, Guo C, Hsieh Y-C, Ye H, Senturk M, Zuo Z, Li Y, Chatterjee S, Botas J, Jackson GR, et al. (2016). Uncoupling neuronal death and dysfunction in Drosophila models of neurodegenerative disease. Acta Neuropathol. Commun 4, 62. [PubMed: 27338814]

Colodner KJ, and Feany MB (2010). Glial fibrillary tangles and JAK/STAT-mediated glial and neuronal cell death in a Drosophila model of glial tauopathy. J. Neurosci. 30, 16102–16113. [PubMed: 21123557]

Cooper TA, Wan L, and Dreyfuss G (2009). RNA and disease. Cell 136, 777–793. [PubMed: 19239895]

Cowan CM, and Mudher A (2013). Are tau aggregates toxic or protective in tauopathies? Front. Neurol. 4, 114. [PubMed: 23964266]

Cowan CM, Bossing T, Page A, Shepherd D, and Mudher A (2010). Soluble hyper-phosphorylated tau causes microtubule breakdown and functionally compromises normal tau in vivo. Acta Neuropathol. 120, 593–604. [PubMed: 20617325]

Cox J, Hein MY, Luber CA, Paron I, Nagaraj N, and Mann M (2014). Accurate proteome-wide label-free quantification by delayed normalization and maximal peptide ratio extraction, termed MaxLFQ. Mol. Cell. Proteomics 13, 2513–2526. [PubMed: 24942700]

Coyle JT, Price DL, and DeLong MR (1983). Alzheimer's disease: a disorder of cortical cholinergic innervation. Science 219, 1184–1190. [PubMed: 6338589]

De Jager PL, Ma Y, McCabe C, Xu J, Vardarajan BN, Felsky D, Klein H-U, White CC, Peters MA, Lodgson B, et al. (2018). A multi-omic atlas of the human frontal cortex for aging and Alzheimer's disease research. Sci. Data 5, 180142. [PubMed: 30084846]

DeNicola AB, and Tang Y (2019). Therapeutic approaches to treat human spliceosomal diseases. Curr. Opin. Biotechnol. 60, 72–81. [PubMed: 30772756]

Dias-Santagata D, Fulga TA, Duttaroy A, and Feany MB (2007). Oxidative stress mediates tau-induced neurodegeneration in Drosophila. J. Clin. Invest 117, 236–245. [PubMed: 17173140]

Dobin A, Davis CA, Schlesinger F, Drenkow J, Zaleski C, Jha S, Batut P, Chaisson M, and Gingeras TR (2013). STAR: ultrafast universal RNA-seq aligner. Bioinformatics 29, 15–21. [PubMed: 23104886]

Dvinge H, and Bradley RK (2015). Widespread intron retention diversifies most cancer transcriptomes. Genome Med. 7, 45. [PubMed: 26113877]

Eftekharzadeh B, Daigle JG, Kapinos LE, Coyne A, Schiantarelli J, Carlomagno Y, Cook C, Miller SJ, Dujardin S, Amaral AS, et al. (2018). Tau Protein Disrupts Nucleocytoplasmic Transport in Alzheimer's Disease. Neuron 99, 925–940.e7. [PubMed: 30189209]

Flickinger TW, and Salz HK (1994). The Drosophila sex determination gene snf encodes a nuclear protein with sequence and functional similarity to the mammalian U1A snRNP protein. Genes Dev. 8, 914–925. [PubMed: 7926776]

Förch P, Puig O, Martínez C, Séraphin B, and Valcárcel J (2002). The splicing regulator TIA-1 interacts with U1-C to promote U1 snRNP recruitment to 5′ splice sites. EMBO J. 21, 6882–6892. [PubMed: 12486009]

Freibaum BD, Chitta RK, High AA, and Taylor JP (2010). Global analysis of TDP-43 interacting proteins reveals strong association with RNA splicing and translation machinery. J. Proteome Res 9, 1104–1120. [PubMed: 20020773]

Garneau NL, Wilusz J, and Wilusz CJ (2007). The highways and byways of mRNA decay. Nat. Rev. Mol. Cell Biol 8, 113–126. [PubMed: 17245413]

Ghosh S, and Feany MB (2004). Comparison of pathways controlling toxicity in the eye and brain in Drosophila models of human neurodegenerative diseases. Hum. Mol. Genet 13, 2011–2018. [PubMed: 15254017]

Gómez-Isla T, Hollister R, West H, Mui S, Growdon JH, Petersen RC, Parisi JE, and Hyman BT (1997). Neuronal loss correlates with but exceeds neurofibrillary tangles in Alzheimer's disease. Ann. Neurol 41, 17–24. [PubMed: 9005861]

Gonsalvez GB, Rajendra TK, Tian L, and Matera AG (2006). The Sm-protein methyltransferase, dart5, is essential for germ-cell specification and maintenance. Curr. Biol 16, 1077–1089. [PubMed: 16753561]

Gramates LS, Marygold SJ, Santos GD, Urbano J-M, Antonazzo G, Matthews BB, Rey AJ, Tabone CJ, Crosby MA, Emmert DB, et al.; the FlyBase Consortium (2017). FlyBase at 25: looking to the future. Nucleic Acids Res. 45 (D1), D663–D671. [PubMed: 27799470]

Gunderson SI, Beyer K, Martin G, Keller W, Boelens WC, and Mattaj LW (1994). The human U1A snRNP protein regulates polyadenylation via a direct interaction with poly(A) polymerase. Cell 76, 531–541. [PubMed: 8313473]

Hales CM, Dammer EB, Diner I, Yi H, Seyfried NT, Gearing M, Glass JD, Montine TJ, Levey AI, and Lah JJ (2014). Aggregates of small nuclear ribonucleic acids (snRNAs) in Alzheimer's disease. Brain Pathol. 24, 344–351. [PubMed: 24571648]

Heppner FL, Ransohoff RM, and Becher B (2015). Immune attack: the role of inflammation in Alzheimer disease. Nat. Rev. Neurosci 16, 358–372. [PubMed: 25991443]

Hsu TY-T, Simon LM, Neill NJ, Marcotte R, Sayad A, Bland CS, Echeverria GV, Sun T, Kurley SJ, Tyagi S, et al. (2015). The spliceosome is a therapeutic vulnerability in MYC-driven cancer. Nature 525, 384–388. [PubMed: 26331541]

Huang da W, Sherman BT, and Lempicki RA (2009a). Bioinformatics enrichment tools: paths toward the comprehensive functional analysis of large gene lists. Nucleic Acids Res. 37, 1–13. [PubMed: 19033363]

Huang da W, Sherman BT, and Lempicki RA (2009b). Systematic and integrative analysis of large gene lists using DAVID bioinformatics resources. Nat. Protoc. 4, 44–57. [PubMed: 19131956]

Humphrey J, Emmett W, Fratta P, Isaacs AM, and Plagnol V (2017). Quantitative analysis of cryptic splicing associated with TDP-43 depletion. BMC Med. Genomics 10, 38. [PubMed: 28549443]

Hyman AA, Weber CA, and Jülicher F (2014). Liquid-liquid phase separation in biology. Annu. Rev. Cell Dev. Biol. 30, 39–58. [PubMed: 25288112]

Ito D, Hatano M, and Suzuki N (2017). RNA binding proteins and the pathological cascade in ALS/FTD neurodegeneration. Sci. Transl. Med 9, eaah5436. [PubMed: 29118263]

Jia Y, Mu JC, and Ackerman SL (2012). Mutation of a U2 snRNA gene causes global disruption of alternative splicing and neurodegeneration. Cell 148, 296–308. [PubMed: 22265417]

Johnson ECB, Dammer EB, Duong DM, Yin L, Thambisetty M, Troncoso JC, Lah JJ, Levey AI, and Seyfried NT (2018). Deep proteomic network analysis of Alzheimer's disease brain reveals alterations in RNA binding proteins and RNA splicing associated with disease. Mol. Neurodegener 13, 52. [PubMed: 30286791]

Kaida D, Berg MG, Younis I, Kasim M, Singh LN, Wan L, and Dreyfuss G (2010). U1 snRNP protects pre-mRNAs from premature cleavage and polyadenylation. Nature 468, 664–668. [PubMed: 20881964]

Khurana V, Elson-Schwab I, Fulga TA, Sharp KA, Loewen CA, Mulkearns E, Tyynelä J, Scherzer CR, and Feany MB (2010). Lysosomal dysfunction promotes cleavage and neurotoxicity of tau in vivo. PLoS Genet. 6, e1001026. [PubMed: 20664788]

Kim HJ, Kim NC, Wang Y-D, Scarborough EA, Moore J, Diaz Z, MacLea KS, Freibaum B, Li S, Molliex A, et al. (2013). Mutations in prion-like domains in hnRNPA2B1 and hnRNPA1 cause multisystem proteinopathy and ALS. Nature 495, 467–473. [PubMed: 23455423]

Lee K-H, Zhang P, Kim HJ, Mitrea DM, Sarkar M, Freibaum BD, Cika J, Coughlin M, Messing J, Molliex A, et al. (2016a). C9orf72 Dipeptide Repeats Impair the Assembly, Dynamics, and Function of Membrane Less Organelles. Cell 167, 774–788.e17. [PubMed: 27768896]

Lee SC-W, Dvinge H, Kim E, Cho H, Micol J-B, Chung YR, Durham BH, Yoshimi A, Kim YJ, Thomas M, et al. (2016b). Modulation of splicing catalysis for therapeutic targeting of leukemia with mutations in genes encoding spliceosomal proteins. Nat. Med 22, 672–678. [PubMed: 27135740]

Lefebvre S, Bürglen L, Reboullet S, Clermont O, Burlet P, Viollet L, Benichou B, Cruaud C, Millasseau P, Zeviani M, et al. (1995). Identification and characterization of a spinal muscular atrophy-determining gene. Cell 80, 155–165. [PubMed: 7813012]

Leichter M, Marko M, Ganou V, Patrinou-Georgoula M, Tora L, and Guialis A (2011). A fraction of the transcription factor TAF15 participates in interactions with a subset of the spliceosomal U1 snRNP complex. Biochim. Biophys. Acta 1814, 1812–1824. [PubMed: 22019700]

Lessing D, and Bonini NM (2009). Maintaining the brain: insight into human neurodegeneration from Drosophila melanogaster mutants. Nat. Rev. Genet 10, 359–370. [PubMed: 19434080]

Li Q, Lee J-A, and Black DL (2007). Neuronal regulation of alternative pre-mRNA splicing. Nat. Rev. Neurosci 8, 819–831. [PubMed: 17895907]

Lin Y, Protter DSW, Rosen MK, and Parker R (2015). Formation and Maturation of Phase-Separated Liquid Droplets by RNA-Binding Proteins. Mol. Cell 60, 208–219. [PubMed: 26412307]

Ling JP, Pletnikova O, Troncoso JC, and Wong PC (2015). TDP-43 repression of nonconserved cryptic exons is compromised in ALS-FTD. Science 349, 650–655. [PubMed: 26250685]

Lorson CL, Hahnen E, Androphy EJ, and Wirth B (1999). A single nucleotide in the SMN gene regulates splicing and is responsible for spinal muscular atrophy. Proc. Natl. Acad. Sci. USA 96, 6307–6311. [PubMed: 10339583]

Love MI, Huber W, and Anders S (2014). Moderated estimation of fold change and dispersion for RNA-seq data with DESeq2. Genome Biol. 15, 550. [PubMed: 25516281]

Luber CA, Cox J, Lauterbach H, Fancke B, Selbach M, Tschopp J, Akira S, Wiegand M, Hochrein H, O'Keeffe M, and Mann M (2010). Quantitative proteomics reveals subset-specific viral recognition in dendritic cells. Immunity 32, 279–289. [PubMed: 20171123]

Lynch DC, Revil T, Schwartzentruber J, Bhoj EJ, Innes AM, Lamont RE, Lemire EG, Chodirker BN, Taylor JP, Zackai EH, et al.; Care4Rare Canada (2014). Disrupted auto-regulation of the spliceosomal gene SNRPB causes cerebro-costo-mandibular syndrome. Nat. Commun. 5, 4483. [PubMed: 25047197]

Majd S, Power J, and Majd Z (2019). Alzheimer's Disease and Cancer: When Two Monsters Cannot Be Together. Front. Neurosci 13, 155. [PubMed: 30881282]

Martinez FJ, Pratt GA, Van Nostrand EL, Batra R, Huelga SC, Kapeli K, Freese P, Chun SJ, Ling K, Gelboin-Burkhart C, et al. (2016). Protein-RNA Networks Regulated by Normal and ALS-Associated Mutant HNRNPA2B1 in the Nervous System. Neuron 92, 780–795. [PubMed: 27773581]

Maziuk BF, Apicco DJ, Cruz AL, Jiang L, Ash PEA, da Rocha EL, Zhang C, Yu WH, Leszyk J, Abisambra JF, et al. (2018). RNA binding proteins co-localize with small tau inclusions in tauopathy. Acta Neuropathol. Commun 6, 71. [PubMed: 30068389]

McAllister G, Amara SG, and Lerner MR (1988). Tissue-specific expression and cDNA cloning of small nuclear ribonucleoprotein-associated polypeptide N. Proc. Natl. Acad. Sci. USA 85, 5296–5300. [PubMed: 2969109]

McKhann G, Drachman D, Folstein M, Katzman R, Price D, and Stadlan EM (1984). Clinical diagnosis of Alzheimer's disease: report of the NINCDS-ADRDA Work Group under the auspices of Department of Health and Human Services Task Force on Alzheimer's Disease. Neurology 34, 939–944. [PubMed: 6610841]

Meier S, Bell M, Lyons DN, Rodriguez-Rivera J, Ingram A, Fontaine SN, Mechas E, Chen J, Wolozin B, LeVine H 3rd., et al. (2016). Pathological Tau Promotes Neuronal Damage by Impairing

Ribosomal Function and Decreasing Protein Synthesis. J. Neurosci 36, 1001–1007. [PubMed: 26791227]

Merlo P, Frost B, Peng S, Yang YJ, Park PJ, and Feany M (2014). p53 prevents neurodegeneration by regulating synaptic genes. Proc. Natl. Acad. Sci. USA 111, 18055–18060. [PubMed: 25453105]

Molliex A, Temirov J, Lee J, Coughlin M, Kanagaraj AP, Kim HJ, Mittag T, and Taylor JP (2015). Phase separation by low complexity domains promotes stress granule assembly and drives pathological fibrillization. Cell 163, 123–133. [PubMed: 26406374]

Mostafavi S, Gaiteri C, Sullivan SE, White CC, Tasaki S, Xu J, Taga M, Klein H-U, Patrick E, Komashko V, et al. (2018). A molecular network of the aging human brain provides insights into the pathology and cognitive decline of Alzheimer's disease. Nat. Neurosci 21, 811–819. [PubMed: 29802388]

Mudher A, Shepherd D, Newman TA, Mildren P, Jukes JP, Squire A, Mears A, Drummond JA, Berg S, MacKay D, et al. (2004). GSK-3β inhibition reverses axonal transport defects and behavioural phenotypes in Drosophila. Mol. Psychiatry 9, 522–530. [PubMed: 14993907]

Nagarkar-Jaiswal S, DeLuca SZ, Lee P-T, Lin W-W, Pan H, Zuo Z, Lv J, Spradling AC, and Bellen HJ (2015a). A genetic toolkit for tagging intronic MiMIC containing genes. eLife 4, e08469.

Nagarkar-Jaiswal S, Lee P-T, Campbell ME, Chen K, Anguiano-Zarate S, Gutierrez MC, Busby T, Lin W-W, He Y, Schulze KL, et al. (2015b). A library of MiMICs allows tagging of genes and reversible, spatial and temporal knockdown of proteins in Drosophila. eLife 4, e05338.

National Institute on Aging, Reagan Institute Working Group on Diagnostic Criteria for the Neuropathological Assessment of Alzheimer's Disease (1997). Consensus Recommendations for the Postmortem Diagnosis of Alzheimer's Disease. Neurobiol. Aging 18, S1–S2. [PubMed: 9330978]

Neumann M, Sampathu DM, Kwong LK, Truax AC, Micsenyi MC, Chou TT, Bruce J, Schuck T, Grossman M, Clark CM, et al. (2006). Ubiquitinated TDP-43 in frontotemporal lobar degeneration and amyotrophic lateral sclerosis. Science 314, 130–133. [PubMed: 17023659]

Nott TJ, Petsalaki E, Farber P, Jervis D, Fussner E, Plochowietz A, Craggs TD, Bazett-Jones DP, Pawson T, Forman-Kay JD, and Baldwin AJ (2015). Phase transition of a disordered nuage protein generates environmentally responsive membraneless organelles. Mol. Cell 57, 936–947. [PubMed: 25747659]

Owald D, and Waddell S (2015). Olfactory learning skews mushroom body output pathways to steer behavioral choice in Drosophila. Curr. Opin. Neurobiol 35, 178–184. [PubMed: 26496148]

Patel A, Lee HO, Jawerth L, Maharana S, Jahnel M, Hein MY, Stoynov S, Mahamid J, Saha S, Franzmann TM, et al. (2015). A Liquid-to-Solid Phase Transition of the ALS Protein FUS Accelerated by Disease Mutation. Cell 162, 1066–1077. [PubMed: 26317470]

Pilla E, Schneider K, and Bertolotti A (2017). Coping with Protein Quality Control Failure. Annu. Rev. Cell Dev. Biol 33, 439–465. [PubMed: 28992440]

Pohl A, and Beato M (2014). bwtool: a tool for bigWig files. Bioinformatics 30, 1618–1619. [PubMed: 24489365]

Polymenidou M, Lagier-Tourenne C, Hutt KR, Huelga SC, Moran J, Liang TY, Ling S-C, Sun E, Wancewicz E, Mazur C, et al. (2011). Long pre-mRNA depletion and RNA missplicing contribute to neuronal vulnerability from loss of TDP-43. Nat. Neurosci 14, 459–468. [PubMed: 21358643]

Prusty AB, Meduri R, Prusty BK, Vanselow J, Schlosser A, and Fischer U (2017). Impaired spliceosomal UsnRNP assembly leads to Sm mRNA down-regulation and Sm protein degradation. J. Cell Biol 216, 2391–2407. [PubMed: 28637748]

Raj B, and Blencowe BJ (2015). Alternative Splicing in the Mammalian Nervous System: Recent Insights into Mechanisms and Functional Roles. Neuron 87, 14–27. [PubMed: 26139367]

Raj T, Li YI, Wong G, Humphrey J, Wang M, Ramdhani S, Wang Y-C, Ng B, Gupta I, Haroutunian V, et al. (2018). Integrative transcriptome analyses of the aging brain implicate altered splicing in Alzheimer's disease susceptibility. Nat. Genet 50, 1584–1592. [PubMed: 30297968]

Ramírez F, Dündar F, Diehl S, Grüning BA, and Manke T (2014). deep-Tools: a flexible platform for exploring deep-sequencing data. Nucleic Acids Res. 42, W187–W191. [PubMed: 24799436]

Saltzman AL, Pan Q, and Blencowe BJ (2011). Regulation of alternative splicing by the core spliceosomal machinery. Genes Dev. 25, 373–384. [PubMed: 21325135]

Salz HK, Mancebo RS, Nagengast AA, Speck O, Psotka M, and Mount SM (2004). The Drosophila U1–70K protein is required for viability, but its arginine-rich domain is dispensable. Genetics 168, 2059–2065. [PubMed: 15611175]

Seyfried NT, Dammer EB, Swarup V, Nandakumar D, Duong DM, Yin L, Deng Q, Nguyen T, Hales CM, Wingo T, et al. (2017). A Multi-network Approach Identifies Protein-Specific Co-expression in Asymptomatic and Symptomatic Alzheimer's Disease. Cell Syst. 4, 60–72.e4. [PubMed: 27989508]

Shen S, Park JW, Lu ZX, Lin L, Henry MD, Wu YN, Zhou Q, and Xing Y (2014). rMATS: robust and flexible detection of differential alternative splicing from replicate RNA-Seq data. Proc. Natl. Acad. Sci. USA 111, E5593–E5601. [PubMed: 25480548]

Shulman JM, and Feany MB (2003). Genetic modifiers of tauopathy in Drosophila. Genetics 165, 1233–1242. [PubMed: 14668378]

Shulman JM, Chipendo P, Chibnik LB, Aubin C, Tran D, Keenan BT, Kramer PL, Schneider JA, Bennett DA, Feany MB, and De Jager PL (2011). Functional screening of Alzheimer pathology genome-wide association signals in Drosophila. Am. J. Hum. Genet. 88, 232–238. [PubMed: 21295279]

Shulman JM, Imboywa S, Giagtzoglou N, Powers MP, Hu Y, Devenport D, Chipendo P, Chibnik LB, Diamond A, Perrimon N, et al. (2014). Functional screening in Drosophila identifies Alzheimer's disease susceptibility genes and implicates Tau-mediated mechanisms. Hum. Mol. Genet 23, 870–877. [PubMed: 24067533]

Snel B, Lehmann G, Bork P, and Huynen MA (2000). STRING: a webserver to retrieve and display the repeatedly occurring neighbourhood of a gene. Nucleic Acids Res. 28, 3442–3444. [PubMed: 10982861]

Spires-Jones TL, and Hyman BT (2014). The intersection of amyloid beta and tau at synapses in Alzheimer's disease. Neuron 82, 756–771. [PubMed: 24853936]

Sreedharan J, Blair IP, Tripathi VB, Hu X, Vance C, Rogelj B, Ackerley S, Durnall JC, Williams KL, Buratti E, et al. (2008). TDP-43 mutations in familial and sporadic amyotrophic lateral sclerosis. Science 319, 1668–1672. [PubMed: 18309045]

Sun S, Ling S-C, Qiu J, Albuquerque CP, Zhou Y, Tokunaga S, Li H, Qiu H, Bui A, Yeo GW, et al. (2015). ALS-causative mutations in FUS/TLS confer gain and loss of function by altered association with SMN and U1-snRNP. Nat. Commun 6, 6171. [PubMed: 25625564]

Tan Q, Yalamanchili HK, Park J, De Maio A, Lu H-C, Wan Y-W, White JJ, Bondar VV, Sayegh LS, Liu X, et al. (2016). Extensive cryptic splicing upon loss of RBM17 and TDP43 in neurodegeneration models. Hum. Mol. Genet 25, 5083–5093. [PubMed: 28007900]

Tollervey JR, Wang Z, Hortobágyi T, Witten JT, Zarnack K, Kayikci M, Clark TA, Schweitzer AC, Rot G, Curk T, et al. (2011). Analysis of alternative splicing associated with aging and neurodegeneration in the human brain. Genome Res. 21, 1572–1582. [PubMed: 21846794]

Tyanova S, Temu T, Sinitcyn P, Carlson A, Hein MY, Geiger T, Mann M, and Cox J (2016). The Perseus computational platform for comprehensive analysis of (prote)omics data. Nat. Methods 13, 731–740. [PubMed: 27348712]

van Gelder CW, Gunderson SI, Jansen EJ, Boelens WC, Polycarpou- Schwarz M, Mattaj IW, and van Venrooij WJ (1993). A complex secondary structure in U1A pre-mRNA that binds two molecules of U1A protein is required for regulation of polyadenylation. EMBO J. 12, 5191–5200. [PubMed: 8262062]

Vance C, Rogelj B, Hortobágyi T, De Vos KJ, Nishimura AL, Sreedharan J, Hu X, Smith B, Ruddy D, Wright P, et al. (2009). Mutations in FUS, an RNA processing protein, cause familial amyotrophic lateral sclerosis type 6. Science 323, 1208–1211. [PubMed: 19251628]

Vanderweyde T, Apicco DJ, Youmans-Kidder K, Ash PEA, Cook C, Lummertz da Rocha E, Jansen-West K, Frame AA, Citro A, Leszyk JD, et al. (2016). Interaction of tau with the RNA-Binding Protein TIA1 Regulates tau Pathophysiology and Toxicity. Cell Rep. 15, 1455–1466. [PubMed: 27160897]

Venken KJ, Schulze KL, Haelterman NA, Pan H, He Y, Evans-Holm M, Carlson JW, Levis RW, Spradling AC, Hoskins RA, and Bellen HJ (2011). MiMIC: a highly versatile transposon

insertion resource for engineering Drosophila melanogaster genes. Nat. Methods 8, 737–743. [PubMed: 21985007]

Wegmann S, Eftekharzadeh B, Tepper K, Zoltowska KM, Bennett RE, Dujardin S, Laskowski PR, MacKenzie D, Kamath T, Commins C, et al. (2018). Tau protein liquid-liquid phase separation can initiate tau aggregation. EMBO J. 37, e98049. [PubMed: 29472250]

Will CL, and Lührmann R (2011). Spliceosome structure and function. Cold Spring Harb. Perspect. Biol 3, a003707.

Wittmann CW, Wszolek MF, Shulman JM, Salvaterra PM, Lewis J, Hutton M, and Feany MB (2001). Tauopathy in Drosophila: neurodegeneration without neurofibrillary tangles. Science 293, 711–714. [PubMed: 11408621]

Yalamanchili HK, Wan Y-W, and Liu Z (2017). Data Analysis Pipeline for RNA-seq Experiments: From Differential Expression to Cryptic Splicing. Curr. Protoc. Bioinformatics 58, 11.15.1–11.15.21.

Yeo G, and Burge CB (2004). Maximum entropy modeling of short sequence motifs with applications to RNA splicing signals. J. Comput. Biol 11, 377–394. [PubMed: 15285897]

Yin S, Lopez-Gonzalez R, Kunz RC, Gangopadhyay J, Borufka C, Gygi SP, Gao F-B, and Reed R (2017). Evidence that C9ORF72 Dipeptide Repeat Proteins Associate with U2 snRNP to Cause Mis-splicing in ALS/FTD Patients. Cell Rep. 19, 2244–2256. [PubMed: 28614712]

Yoshida K, Sanada M, Shiraishi Y, Nowak D, Nagata Y, Yamamoto R, Sato Y, Sato-Otsubo A, Kon A, Nagasaki M, et al. (2011). Frequent pathway mutations of splicing machinery in myelodysplasia. Nature 478, 64–69. [PubMed: 21909114]

Zhang B, Kirov S, and Snoddy J (2005). WebGestalt: an integrated system for exploring gene sets in various biological contexts. Nucleic Acids Res. 33, W741–W748. [PubMed: 15980575]

Zhang Z, Lotti F, Dittmar K, Younis I, Wan L, Kasim M, and Dreyfuss G (2008). SMN deficiency causes tissue-specific perturbations in the repertoire of snRNAs and widespread defects in splicing. Cell 133, 585–600. [PubMed: 18485868]

Highlights

- Genetic manipulation of the spliceosome enhances Tau neurotoxicity in flies
- Mutation of the core spliceosome factor, *SmB*, causes progressive neurodegeneration
- The Tau and *SmB* transcriptomes share similar profiles of RNA-splicing errors
- Alzheimer's disease Tau pathology associates with cryptic splicing errors in human brains

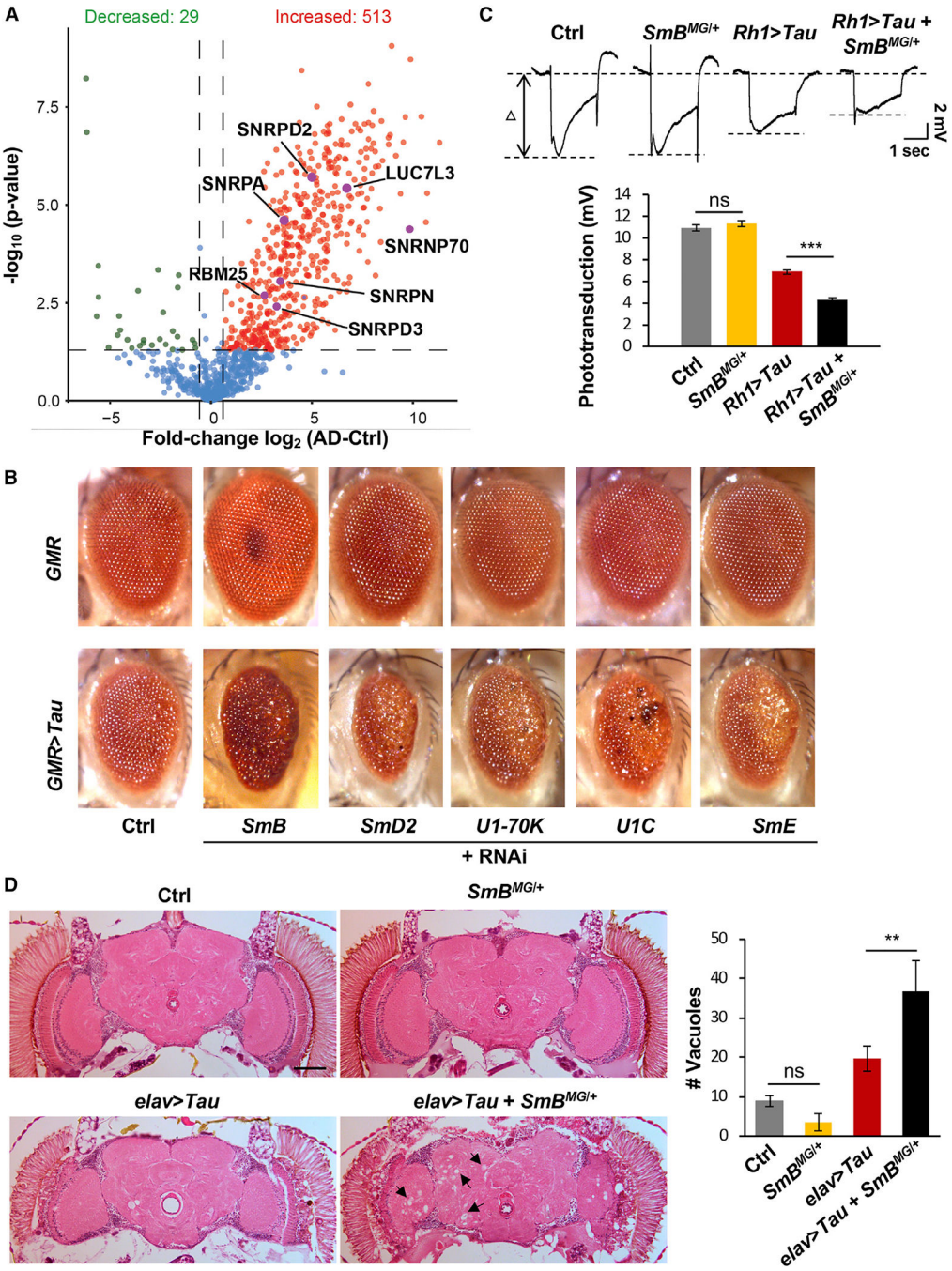

Figure 1. Tau Associates and Genetically Interacts with Spliceosomal Factors

(A) Following coimmunoprecipitation, 1,065 Tau-associated proteins were identified from AD or control postmortem brain tissue homogenates (n = 4 each). Volcano plot highlights proteins showing >1.5-fold increased (red) or decreased (green) interactions with Tau in AD (all $p < 0.05$), including numerous ribonucleoproteins ($p = 7.7 \times 10^{-5}$). Spliceosome components are denoted. See also Figure S1, Tables S1, and Data S1, tabs i and ii.

(B) Compared with controls (Ctrl, top left), Tau^{V337M} expression in the eye (*GMR-GAL4*) causes reduced eye size and roughened surface (bottom left: 1.98 ± 0.08, mean score ±

SEM, n > 35 for all genotypes), and RNAi targeting spliceosome factors enhanced toxicity (bottom row, $p < 0.0001$: *SmB*, 3.67 ± 0.06; *SmD2*, 4.00 ± 0.00; *U1–70K*, 4.04 ± 0.03; *U1C*, 3.92 ± 0.09; and *SmE*, 4.00 ± 0.00). RNAi lines were non-toxic when expressed independently (top row). See also Data S1, tab iii.

(C) Tau^{WT} expression in the adult retina (*Rh1-GAL4*) causes reduced electroretinogram (ERG) amplitude in 5-day-old flies, and this phenotype is enhanced in SmB^{MG} heterozygotes (n > 10 for quantification). See also Figures S2A–S2C.

(D) Pan-neuronal expression of Tau^{R406W} (*elav-GAL4*) causes progressive neuropil vacuolization (arrows) in hematoxylin and eosin-stained frontal brain sections in 10-day-old adult flies, and this phenotype is enhanced in SmB^{MG} heterozygotes (n > 8 for quantification). Scale bar: 50 μm. See also Figures S2D and S2E. All error bars denote mean ± SEM. **p < 0.01; ***p < 0.001; ns, not significant.

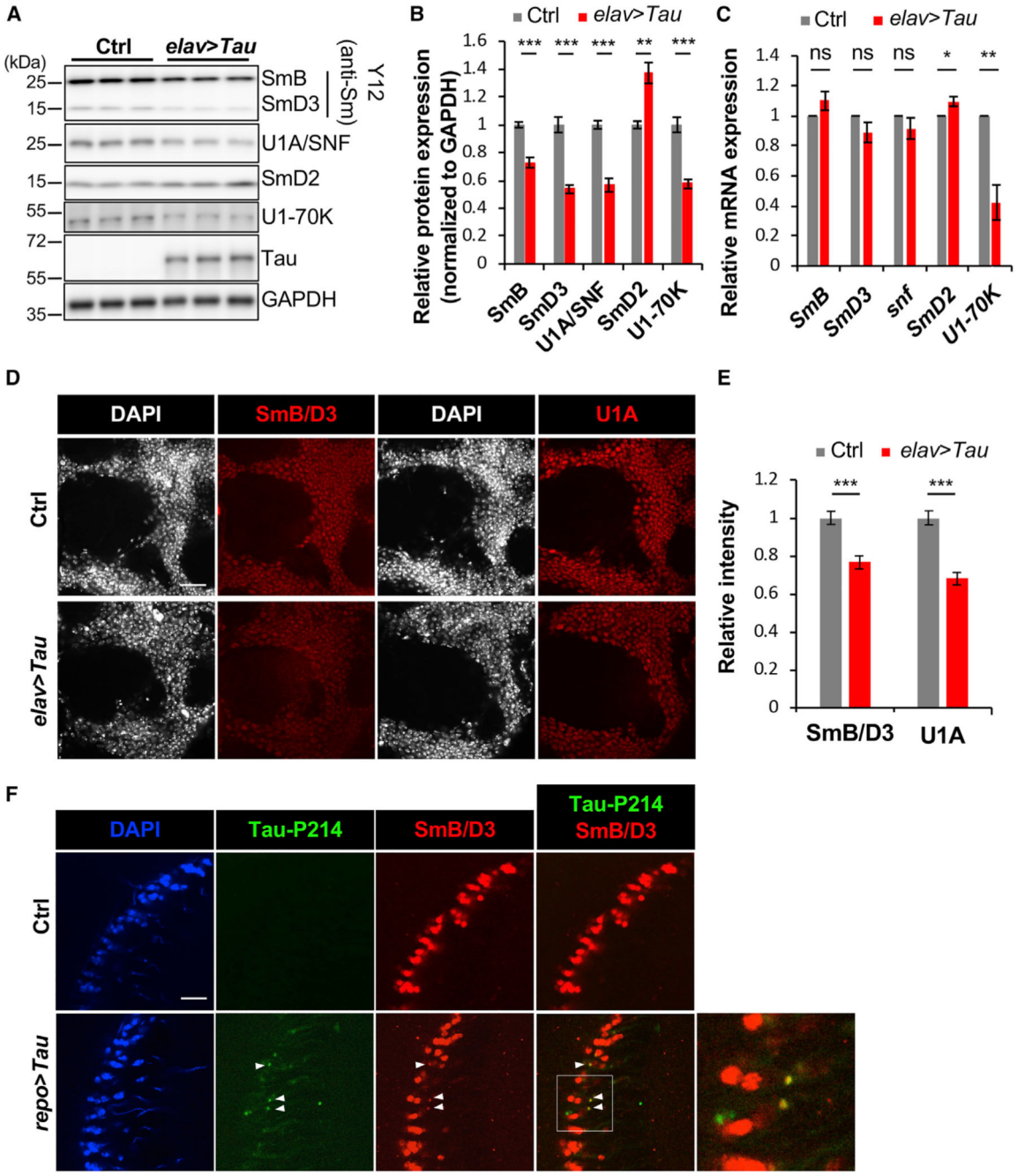

Figure 2. Disruption of the Spliceosome following Tau Expression in *Drosophila*

(A and B) Pan-neuronal human Tau^{R406W} disrupts expression of multiple spliceosomal proteins in 1-day-old adult fly head homogenates. Western blots (A) were probed for Tau or spliceosome proteins and normalized to the loading control, GAPDH (n = 4 replicates for quantification, B). The Y12 antibody recognizes both SmB and SmD3.

(C) mRNA expression was also examined in 1-day-old adult heads (n = 3).

(D and E) Whole-mount stains of 1-day-old adult fly brains (D) reveal depletion of SmB/D3 and U1A/SNF protein (red, n = 15 for quantification, E). Nuclei are colabeled with 4′,6-diamidino-2-phenylindole (DAPI; grayscale). Scale bar: 20 μm.

(F) Glial expression of Tau^{WT} (*repo-GAL4*) induces cytoplasmic foci (arrowheads) of SmB/D3 (Y12, red) that colocalize with phospho-Tau aggregates (green) in 10-day-old adult brains. Nuclei are labeled with DAPI (blue). Boxed region is magnified at right. Quantification ($n > 9$) reveals 14.86% ± 2.3% of phospho-Tau aggregates colabeling for Sm proteins; aggregates were not observed in controls. Scale bar: 10 μm. See also Figure S3A. All error bars denote mean ± SEM. *$p < 0.05$; **$p < 0.01$; ***$p < 0.001$; ns, not significant.

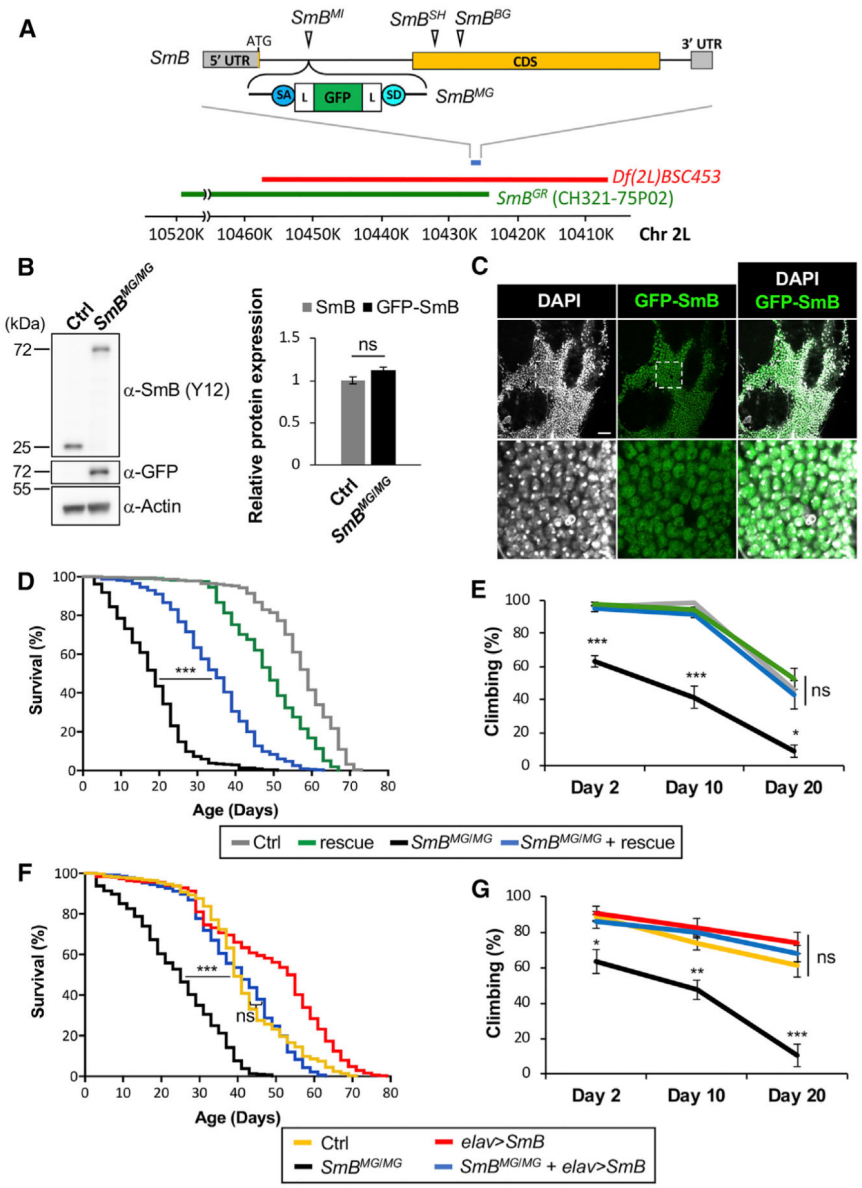

Figure 3. Loss of *SmB*, Encoding a Core Spliceosome Factor, Causes Reduced Survival and Progressive Locomotor Impairment

(A) The *SmB* locus, including single coding exon (CDS, yellow), untranslated regions (UTRs, gray), and transposable elements. To generate SmB^{MG}, recombination-mediated cassette exchange was performed using SmB^{MI}, introducing a coding exon for GFP, flanked by flexible linkers (Ls) and splice acceptor and donor sequences (SA/SDs). The deficiency strain (red), *Df(2L)BSC453*, deletes ~51 kb including the entire *SmB* locus. The transgenic genomic rescue strain, SmB^{GR}, carries a ~90-kb bacterial artificial chromosome (BAC, CH321–75P02, green), including *SmB.* See also Table S2.

(B) $SmB^{MG/MG}$ homozygotes demonstrate expression of the GFP-SmB fusion protein at levels comparable with controls (n = 3 for quantification, SmB protein normalized to Actin).

(C) GFP-SmB (green) is localized to the nucleus (DAPI, grayscale) in brains from $SmB^{MG/MG}$ adults. Scale bar: 20 μm. Boxed region (top) is magnified below.

(D) *SmB*$^{MG/MG}$ adults (black) exhibit reduced survival and this phenotype is partially rescued by the *SmB* genomic rescue (blue) (n > 313 per genotype). See also Figure S4A.
(E) *SmB*$^{MG/MG}$ adults also manifest progressive locomotor impairment (n > 5 groups). See also Figure S4B.
(F and G) Both the *SmB*$^{MG/MG}$ survival (F, n > 288) and locomotor (G, n > 4 groups) phenotypes were rescued by pan-neuronal expression of wild-type *SmB*.
All error bars denote mean ± SEM. *p < 0.05; **p < 0.01; ***p < 0.001; ns, not significant.

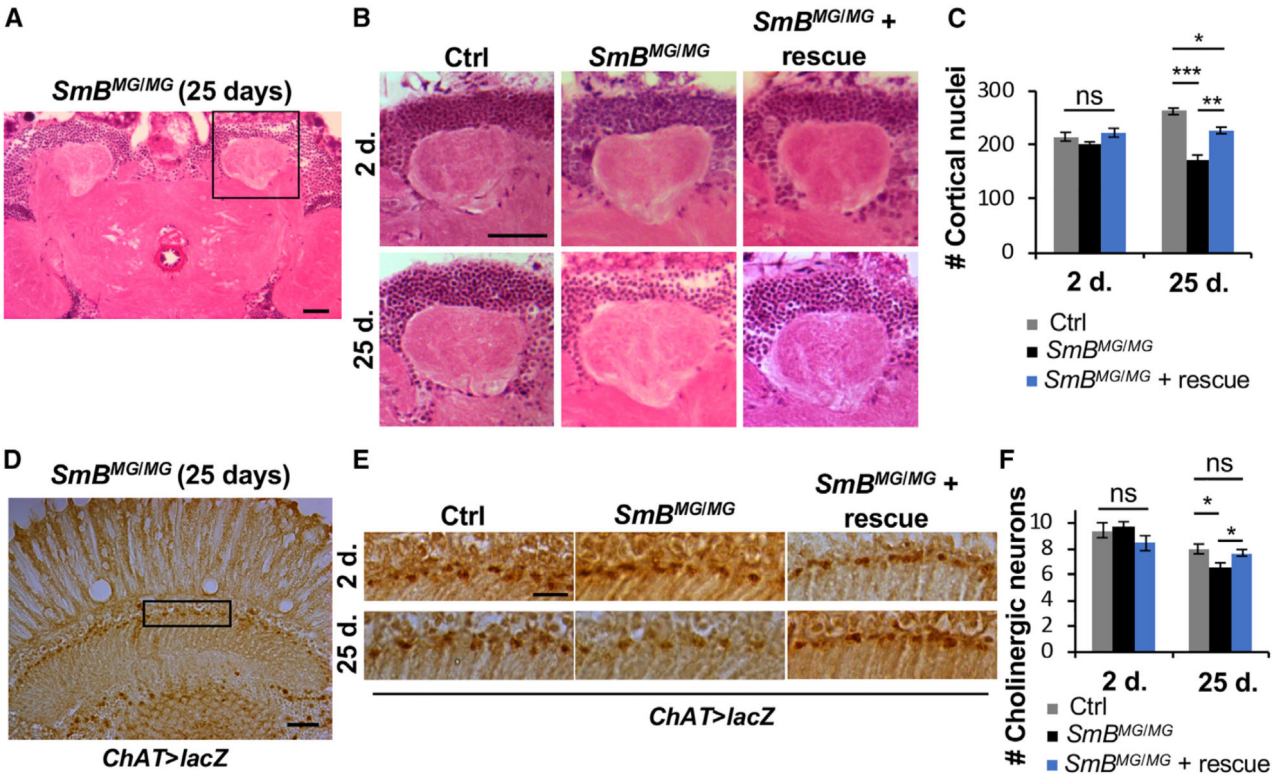

Figure 4. Loss of *SmB* Causes Neurodegeneration

(A) Hematoxylin and eosin-stained frontal brain section at the level of mushroom body calyx, highlighting the region of interest for (B) and (C). Scale bar: 25 μm.

(B and C) *SmB*$^{MG/MG}$ adults (B) show progressive loss of cortical nuclei between 2 and 25 days of age (n > 5 for quantification, C). Scale bar: 25 μm.

(D) Frontal section at the level of lamina highlighting region of interest for (E) and (F) and DAB-positive cholinergic neurons (*ChAT>lacZ* reporter). Scale bar: 20 μm.

(E and F) *SmB*$^{MG/MG}$ animals (E) exhibit cholinergic neuron loss between 2 and 25 days (n > 9 for quantification, F). Scale bar: 10 μm.

All error bars denote mean ± SEM. *p < 0.05; **p < 0.01; ***p < 0.001; ns, not significant. See also Figures S4C–S4F and S5.

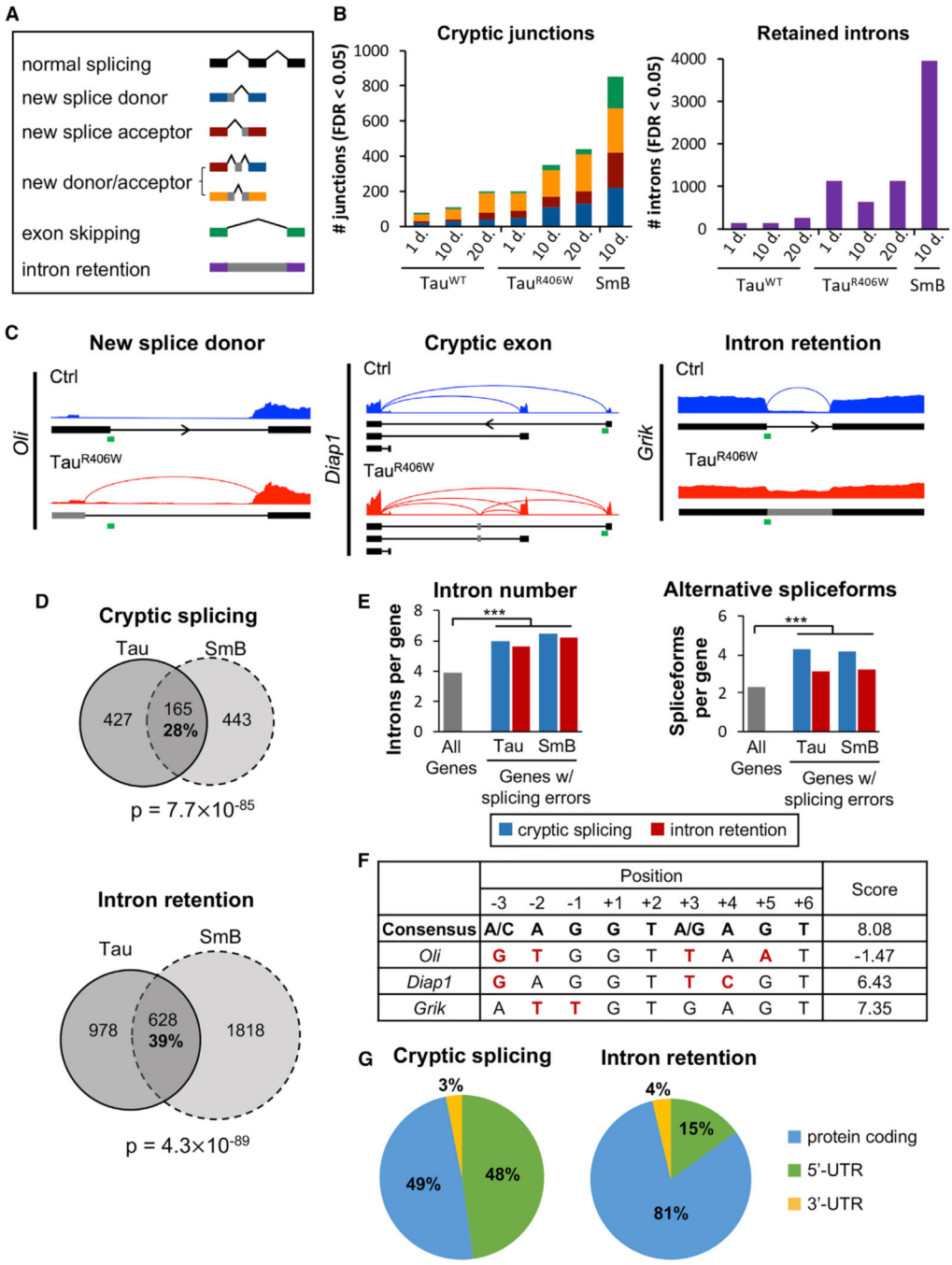

Figure 5. Tau Expression and *SmB* Loss Cause Similar Splicing Errors in *Drosophila* Brains

(A) Key for splicing errors shown in (B).

(B) Pan-neuronal expression of Tau^{WT} or Tau^{R406W} induces differential expression of cryptic splicing errors (left) and intron retention (right), similar to $SmB^{MG/MG}$, based on RNA-seq in 1-, 10-, or 20-day-old flies (n = 3 per genotype, except n = 2 for same-batch control for Tau^{R406W} comparison). See also Figure S6B, Tables S4 and S5, and Data S1, tabs iv and v.

(C) Histograms for representative Tau-induced splicing errors in 20-day-old flies, showing RNA-seq reads normalized between control and Tau^{R406W} and split reads spanning splice junctions. Transcript structures are indicated below, including reference-annotated (black) versus aberrant exons (gray) resulting from cryptic splice junctions. Transcript orientation (arrows) and the 5′-splice donor sites (green bars) analyzed in (F) are denoted. See also Figure S6C.

(D) Genes harboring splicing errors following pan-neuronal expression of Tau^{R406W} (union of 1-, 10-, and 20-day results) strongly overlap with $SmB^{MG/MG}$ (10 days). Percentage denotes Tau-associated, differentially spliced genes that also overlap. See also Figures S6D–S6F.

(E) Splicing errors in Tau^{R406W} transgenic and $SmB^{MG/MG}$ flies occur more commonly in genes with greater numbers of introns (left) or annotated alternatively spliced transcripts (right), compared with all *Drosophila* genes. ***$p < 0.001$.

(F) Splicing errors occur at exon-intron junctions with splice donor sequences that diverge from the consensus motif for U1 spliceosome binding. The consensus splice donor (5′-splice site) sequence (bold) is shown, along with splice donor sequences corresponding to splicing errors in representative genes (green bars in C). Nucleotides that diverge from the consensus are shown (red), along with the splice site binding strength score. See also Figures S7A and S7B.

(G) Many splicing errors in Tau^{R406W} flies affect protein coding sequences (blue) or untranslated regions (UTRs: green, 5′-UTR; yellow: 3′-UTR), and are likely to disrupt protein expression. See also Data S1, tabs vi and vii.

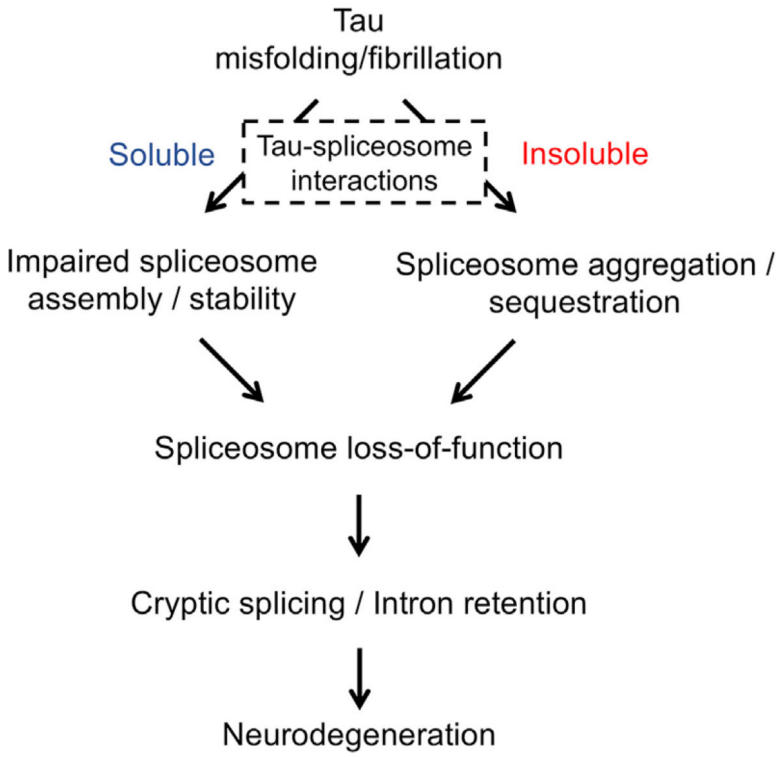

Figure 6. Hypothetical Model for Tau-Spliceosome Interactions in AD

We propose that spliceosome factors can associate with either insoluble or soluble Tau species, respectively, leading to cytoplasmic sequestration or disrupting snRNP assembly and/or stability. Tau-spliceosome interactions likely contribute to splicing errors, global transcriptome perturbation and, ultimately, CNS dysfunction and neuronal loss.

Table 1.

Analyses of Cryptic Load in Human Postmortem Brains

Predictor Variable	Sample Size	Coefficient	p Value
AD diagnosis[a]	620 (241 versus 379)	1.7	0.09
Braak (high or low)[b]	241 (105 versus 136)	2.6	0.01
Tangle burden[c]	600 (300 versus 300)	1.6	0.1
	400 (200 versus 200)	1.8	0.07
	300 (150 versus 150)	2.2	0.03
	200 (100 versus 100)	2.3	0.02
	100 (50 versus 50)	3.0	0.004

[a]Pathologic AD based on National Institute on Aging (NIA)-Reagan.

[b]High or low Braak tangle score (Braak 0–2 versus 5–6).

[c]Neurofibrillary tangle burden, nested case and control analysis considering the extremes of the trait distribution for all samples.

KEY RESOURCES TABLE

REAGENT or RESOURCE	SOURCE	IDENTIFIER
Antibodies		
Purified Mouse IgG2a K isotype	BD PharMingen	Cat# 550339; RRID: AB_393619
Mouse anti-Tau (TAU-5)	Thermo Fisher Scientific	Cat# MA5–12808; RRID: AB_10980631
Rabbit anti-Tau (Tau-E178)	Abcam	Cat# ab32057; RRID: AB_778254
Rabbit anti-Tau	Dako	Cat# A0024; RRID: RRID:AB_10013724
Rabbit anti-Tau[p214]	Invitrogen	Cat# 44–742G; RRID: AB_1502105
Mouse anti-Sm (clone Y12)	Thermo Fisher Scientific	Cat# MA5–13449; RRID: AB_10944191
Mouse anti-SNF	Lab: Dr. Helen K. Salz	N/A
Rabbit anti-SNRPD2	Novus Biologicals	Cat# NBP1–87028; RRID: AB_11005028
Rabbit anti-U1–70K	Lab: Dr. Nicholas Seyfried	N/A
Rabbit anti-GFP	Invitrogen	Cat# A-11122; RRID: AB_221569
Rabbit anti-GAPDH	GeneTex	Cat# 100118; RRID: AB_10723203
Mouse anti-Actin (clone C4)	Millipore	Cat# MAB1501; RRID: AB_2223041
Alexa Fluor 680 Goat anti-Mouse IgG (H+L)	Thermo Fisher Scientific	Cat# A-21058; RRID: AB_2535724
Alexa Fluor 680 Goat anti-Rabbit IgG (H+L)	Thermo Fisher Scientific	Cat# A-21109; RRID: AB_2535758
Alexa Fluor 790 Donkey anti-Mouse IgG (H+L)	Thermo Fisher Scientific	Cat# A-11371; RRID: AB_2534144
Alexa Fluor 790 Donkey anti-Rabbit IgG (H+L)	Thermo Fisher Scientific	Cat# A-11374; RRID: AB_2534145
Cy3-conjugated Goat anti-mouse IgG	Jackson ImmunoResearch	Cat# 115–165–146; RRID: AB_2338690
Alexa Fluor 488-conjugated goat anti-rabbit IgG	Jackson ImmunoResearch	Cat# 711–545–152; RRID: AB_2313584
Mouse anti-b-galactosidase	Promega	Cat# Z3783; RRID: AB_430878
Mouse anti-elav	Developmental Studies Hybridoma Bank	Cat# Elav-9F8A9; RRID: AB_528217
Mouse anti-repo	Developmental Studies Hybridoma Bank	Cat# 8D12 anti-Repo; RRID: AB_528448
Goat anti-mouse IgG-HRP	Santa Cruz	Cat# sc-2005; RRID: AB_631736
Goat anti-rabbit IgG-HRP	Santa Cruz	Cat# sc-2004; RRID: AB_631746
Chemicals, Peptides, and Recombinant Proteins		
Protein A-Sepharose conjugated beads	Invitrogen	Cat# 101041
DynaBeads Protein G	Invitrogen	Cat# 1003D
Lysyl endopeptidase (lys-C)	Wako	Cat# 125–05061
Trypsin	Promega	Cat# v5111
Peptide calibration mixture	Thermo Fisher Scientific	Cat# 88321
Protease inhibitor cocktail	Gendepot	Cat# P3100–001
DAB peroxidase substrate	Vector Laboratories	Cat# SK-4100
8% glutaraldehyde	Electron Microscopy Sciences	Cat# 16020
Trizol	Invitrogen	Cat# 15596–026

REAGENT or RESOURCE	SOURCE	IDENTIFIER
DNaseI	Promega	Cat# M6101
2X Laemmli Sample Buffer	Biorad	Cat# 161–0737
ECL	PerkinElmer	Cat# 121001EA
Vectashield mounting medium	Vector Laboratories	Cat# H-1000
Vectashield DAPI-containing mounting medium	Vector Laboratories	Cat# H-1200
Critical Commercial Assays		
Click-iT Plus TUNEL Assay	Invitrogen	Cat# C10617
RNeasy Micro Kit	QIAGEN	Cat# 74104
SuperScript III First-Strand Synthesis System	Invitrogen	Cat# 18080–051
iQ SYBR Green Supermix	Biorad	Cat# 170–8882
ABC Kit	Vector Laboratories	Cat# PK-6200
Deposited Data		
Drosophila RNA-seq data	AMP-AD Knowledge Portal	ID# syn7274101
	https://doi.org/10.7303/syn2580853	https://doi.org/10.7303/syn7274101
ROSMAP human brain RNA-seq data	AMP-AD Knowledge Portal	ID# syn3388564
	https://doi.org/10.7303/syn2580853	https://doi.org/10.7303/syn3388564
Experimental Models: Fly Lines		
ChAT-GAL4	Bloomington Drosophila Stock Center	BDSC_6798
dpp-GAL4	Lab: Dr. Hugo J. Bellen	N/A
repo-GAL4	Lab: Dr. Hugo J. Bellen	N/A
Rh1-GAL4	Lab: Dr. Hugo J. Bellen	N/A
$elav^{C155}$*-GAL4*	Bloomington Drosophila Stock Center	BDSC_458
GMR-GAL4	Lab: Dr. Juan Botas	N/A
UAS-Tau^{WT}	Lab: Dr. Mel B. Feany	N/A
UAS-Tau^{V337M}	Lab: Dr. Mel B. Feany	N/A
UAS-Tau^{R406W}*/TM3*	Lab: Dr. Mel B. Feany	N/A
UAS-lacZ	Lab: Dr. Hugo J. Bellen	N/A
SmB^{BG}*/CyO*	Bloomington Drosophila Stock Center	BDSC_13130
SmB^{MI}*/CyO*	Bloomington Drosophila Stock Center	BDSC_43739
SmB^{SH}*/CyO*	Kyoto Stock Center	KSC_122076
Df(2L)BSC453	Bloomington Drosophila Stock Center	BDSC_24957
SmB^{GR}	GenetiVision	Stock ID# P7-D6
w^{1118}*;* SmB^{MG}*/CyO;* SmB^{GR}*/TM6B*	This paper	N/A
snRNP-U1–70K^{2}*/CyO*	Lab: Dr. Helen K. Salz	N/A
snf^{210}*/FM7*	Lab: Dr. Helen K. Salz	N/A

REAGENT or RESOURCE	SOURCE	IDENTIFIER
repo-GAL4, tub-GAL80^{TS}, UAS-Tau^{WT}/TM3	Lab: Dr. Mel B. Feany	N/A
yw; SmB^{MG}/CyO	This paper	N/A
w^{1118}; SmB^{MG}/CyO	This paper	N/A
UAS-SmB	This paper	N/A
Oligonucleotides		
Primers for PCR-detection of spliceosome mRNAs and validation of splicing errors are listed in Data S1, tab xi	This paper	N/A
Software and Algorithms		
MaxQuant	Cox et al., 2014	https://www.biochem.mpg.de/5111795/maxquant; RRID: SCR_014485
Leica Application Suite X	Leica	https://www.leica-microsystems.com/products/microscope-software/details/product/leica-las-x-ls/; RRID: SCR_013673
ImageJ	National Institute of Health	https://imagej.nih.gov/ij/; RRID: SCR_003073
LabChart Reader	ADInstruments	https://www.adinstruments.com/products/labchart-reader; RRID: N/A
Picard	Broad Institute	https://broadinstitute.github.io/picard/; RRID: SCR_006525
FastQC v0.10.1	Andrews, 2010	http://www.bioinformatics.babraham.ac.uk/projects/fastqc/; RRID: SCR_014583
STAR 2.5.3a	Dobin et al., 2013	https://github.com/alexdobin/STAR; RRID: SCR_015899
rMATS	Shen et al., 2014	http://rnaseq-mats.sourceforge.net/; RRID: SCR_013049
DESeq2	Love et al., 2014	https://bioconductor.org/packages/release/bioc/html/DESeq2.html; RRID: SCR_015687
MaxEntScan	Yeo and Burge, 2004	https://genes.mit.edu/burgelab/maxent/Xmaxentscan_scoreseq.html; RRID: SCR_016707
DeepTools	Ramírez et al., 2014	https://deeptools.readthedocs.io/en/develop/; RRID: SCR_016366
Bwtool	Pohl and Beato, 2014	http://cromatina.crg.eu/bwtool; RRID: SCR_003035
DEIn	This paper	https://www.liuzlab.org/Scripts_DEIn.zip
CrypSplice	This paper	https://www.liuzlab.org/Scripts_Tau-SmB.zip
CrypticLoad	This paper	https://ww.liuzlab.org/Scripts_CrypticLoad.zip
DAVID v6.8	Huang da et al., 2009b	https://david.abcc.ncifcrf.gov/; RRID: SCR_001881
WebGestalt	Zhang et al., 2005	http://www.webgestalt.org/option.php; RRID:SCR_006786
Other		
Orbitrap Fusion Tribrid Mass Spectrometer	Thermo Fisher Scientific	N/A
CFX96 Touch Real-Time PCR Detection System	Biorad	N/A
Leica SP8 confocal microscope	Leica	N/A
Leica EC3 system	Leica	N/A
Leica DM 6000 B system	Leica	N/A